

# CFD-driven Symbolic Identification of Algebraic Reynolds-Stress Models

Ismail BEN HASSAN SAÏDI<sup>a,\*</sup>, Martin SCHMELZER<sup>b</sup>, Paola CINNELLA<sup>c</sup>,  
Francesco GRASSO<sup>d</sup>

<sup>a</sup>*Institut Aérotechnique, CNAM, 15 Rue Marat, 78210 Saint-Cyr-l'École, France*

<sup>b</sup>*Faculty of Aerospace Engineering, Delft University of Technology, Kluyverweg 2, Delft, The Netherlands*

<sup>c</sup>*Institut Jean Le Rond D'Alembert, Sorbonne Université, 4 Place Jussieu, 75005 Paris, France*

<sup>d</sup>*Laboratoire DynFluid, CNAM, 151 Boulevard de l'Hopital, 75013 Paris, France*

---

## Abstract

A CFD-driven deterministic symbolic identification algorithm for learning explicit algebraic Reynolds-stress models (EARSM) from high-fidelity data is developed building on the CFD-free SpARTA algorithm of [1]. Corrections for the Reynolds stress tensor and the production of transported turbulent quantities of a baseline linear eddy viscosity model (LEVM) are expressed as functions of tensor polynomials selected from a library of candidate functions. The CFD-driven training consists in solving a blackbox optimization problem in which the fitness of candidate EARSM models is evaluated by running RANS simulations. A preliminary sensitivity analysis is used to identify the most influential terms and to reduce the dimensionality of the search space and the Constrained Optimization using Response Surface (CORS) algorithm, which approximates the black-box cost function using a response surface constructed from a limited number of CFD solves, is used to find the optimal model parameters within a realizable search space. The resulting turbulence models are numerically robust and ensure conservation of mean kinetic energy. Furthermore, the CFD-driven procedure enables training of models against any target quantity of interest computable as an output of the CFD model. Model discovery and cross-validation is performed for three configurations of 2D turbulent separated flows in channels of variable section using different sets of training data to show the flexibility of the method. The discovered models are then applied to the prediction of an unseen 2D separated flow with higher Reynolds number and different geometry. The predictions of the discovered models for the new case are shown to be not only more accurate of the baseline LEVM, but also of a multi-purpose EARSM model derived from purely physical arguments. The proposed deterministic symbolic identification approach constitutes a promising candidate for

---

\*Corresponding author

*Email address:* ismail.benhassansaidi@ensam.eu (Ismail BEN HASSAN SAÏDI)

building accurate and robust RANS models customized for a given class of flows for a moderate computational cost.

*Keywords:* `elsarticle.cls`, L<sup>A</sup>T<sub>E</sub>X, Elsevier, template  
*2010 MSC:* 00-01, 99-00

---

## 1. Introduction

Computational Fluid Dynamics (CFD) simulations of turbulent flows for industrial applications largely rely on the Reynolds-Averaged Navier-Stokes (RANS) equations supplemented with linear eddy viscosity models (LEVM) for the Reynolds stresses. Despite their generally inaccurate predictions of non-equilibrium turbulent flow with strong pressure gradients, streamline curvature, anisotropy and separation [2, 3] LEVM are usually preferred to more sophisticated models –namely, Reynolds stress models (RSM)– due to their superior robustness and lower computational cost. RSM involve additional transport equations for the Reynolds stresses [4, 5, 6], which in principle can be derived exactly from the Navier–Stokes equations. Unfortunately, this process introduces a number of additional unclosed terms (pressure-strain correlations, diffusion and dissipation rates) that need suitable mathematical modeling, as well as the calibration of the associated closure coefficients. The predictive performance and the numerical robustness of RSM is sensitive to the modeling of these terms. Furthermore, RSM involve the solution of seven additional transport equations (for 3D flows), thus increasing computational cost compared to LEVM.

A trade-off between LEVM and RSM consists in the development of so-called generalized eddy viscosity models [7]. Within this class of models, Explicit Algebraic Reynolds Stress Models (EARSM) generalize the linear eddy viscosity concept by assuming that the anisotropic part of the Reynolds stress not only depends on the mean strain rate tensor  $S_{ij}$  but also on the rotation rate tensor  $\Omega_{ij}$  through a non linear relationship. Specifically, Reynolds stress anisotropy is written as a tensor polynomial of  $S_{ij}$  and  $\Omega_{ij}$  [7], the coefficients of which can be determined from the RSM equations simplified under local equilibrium [8] as functions of tensor invariants. In this sense, classical EARSM partly inherit from modeling hypothesis used for the development of RSM. Furthermore, they also require the calibration of a number of closure coefficients, which is usually done for a set of simple canonical flows. Due to the uncertainties associated with the choice of both the mathematical structure and the closure coefficients the EARSM, as well as other RANS models, are not universally valid and may perform poorly for flow configurations very dissimilar to the calibration ones. The reader may refer to [9] for a discussion of RANS modeling uncertainties.

Several recent studies have illustrated the potential of data-driven approaches for the development of turbulence models, customized for specific classes of flows (see, e.g., [10, 9]). Such approaches use machine learning techniques to infer the functional form of the Reynolds stress tensor from high-fidelity experimental or,

most often, numerical data. While many of them use black-box machine learning such as Deep Neural Networks to reconstruct or correct the Reynolds stress tensor, some others have considered open-box machine learning techniques, relying on the use of a wisely chosen library of candidate functions to build physically interpretable turbulence models similar to EARSM. In [11], this goal is achieved by using non deterministic symbolic regression based on an evolutionary algorithm (Gene Expression Programming, GEP). The GEP is efficient in constructing models with improved accuracy for separated flows. Moreover, learned models involving only a few nonlinear terms are found to exhibit lower training and prediction error and higher numerical robustness [12, 13]. However, the random nature of the search algorithm discovers a model with a different mathematical form at each run, using the same training data. A deterministic symbolic identification algorithm called SpaRTA (Sparse Regression of Turbulent Stress Anisotropy) has been proposed in [1]. SpaRTA combines functions from a predefined library of candidates without any random recombination. The algorithm constrains the search towards algebraic models of minimal complexity using sparsity-promoting regression techniques [14, 15]. This method has also shown its efficiency in improving RANS models for the simulation of separated flows behind steps or in convergent-divergent channels. Recently, SpaRTA has been coupled with LES in a multi-fidelity optimization framework, allowing significant improvements over designs based on a simple LEVM [16]. A similar deterministic identification approach has been also proposed in [17], whereby unclosed tensors in the RANS or Reynolds-stress transport equations are written as linear combinations of a tensor basis, whose coefficients are learned from synthetic or DNS data of simple flows using  $l_1$ -constrained mean square regression. The results are compared to a constitutive law using a similar decomposition, but with coefficients built on Neural Networks (NN) [18]. Because the deterministic identification methodology seeks to uncover underlying physics, far less data is required to achieve reasonable learned models. As a consequence, it represents potentially an excellent modeling construct for sparse datasets, such as those available from experiments.

A limitation of the above-mentioned symbolic identification algorithms relies in their training procedure. The latter uses a frozen-field (or CFD-free) mode, whereby frozen mean-field and Reynolds stress high-fidelity data are used to train the constitutive equation for the Reynolds stresses. Once the training is completed, the resulting model is plugged within a CFD solver and used to predict a new flow. Such a strategy has the advantage of simplicity and extremely low cost (no CFD solves are required for the training procedure). The drawbacks are: 1) the need for full-field, high quality data for first and second-order flow statistics (namely, the Reynolds stresses), which are not always promptly available; 2) due to the offline training, the learned model may cause numerical stiffness once coupled with a CFD code and require the introduction of relaxation coefficients [1] or implicit treatment [17] to stabilize the CFD calculations and improve their conditioning; 3) offline training using a frozen mean field does not guarantee exact conservation of mechanical energy.

The above-mentioned limitations can be overcome by adopting a CFD-driven

training procedure. In such an approach, the fitness of candidate EARSIM models is evaluated by running RANS simulations. This is expected to enable flexible use of incomplete or noisy training data for any flow quantity at hand. Moreover as each candidate model is evaluated through a RANS simulation, models preventing the convergence of the solution can be eliminated during the training process. Hence, learned models are expected to be robust. Finally, the CFD-driven approach ensures coupling of the mean field and turbulent transport equations at any stage of the training process, thus guaranteeing the conservation of mean kinetic energy. However, the price to pay is a much higher computational cost of the training procedure, due to the multiple CFD solves required to evaluate model fitness. A promising CFD-driven formulation of the GEP method of [11] has been recently proposed in [19]. Besides its non deterministic nature, candidate models in GEP need to iterate through hundreds or thousands of generations to get the desired models, making the overall cost of training quite high.

In the present paper, we propose a CFD-driven extension of the SpARtA algorithm [1] that evaluates the fitness of candidate models by running RANS simulations. The new method generates data-driven EARSIM of the same general form of the CFD-free SpARtA by using potentially any kind of training data. In order to drastically reduce the computational burden associated with model training in a highly dimensional parameter space, a preliminary local sensitivity analysis is used to identify the most influential parameters. Subsequently, a pre-screening of candidate models is carried out using the Reynolds stress anisotropy barycentric map representation [20], so that parameter ranges leading to violation of the realizability conditions are discarded. Finally, a response surface methodology [21] is used to construct an inexpensive surrogate of the costly black-box function from a moderate number of CFD evaluations. An approximate solution to the optimization problem is then computed by running the optimizer on the response surface. As in the CFD-free SpARtA approach, the turbulence models obtained at the end of the procedure are data-driven EARSIM models involving a subset of the initial library of candidate functions. Numerical experiments for selected separated flows are used to illustrate the accuracy and the generalization capabilities of the models.

The paper is organized as follows. In Section 2, we briefly recall the formulation of LEVM and EARSIM models of turbulence. Datasets used for model training and validation are described in Section 3. In Section 4, we recall the main features of the CFD-free SpARtA algorithm. Section 5 is devoted to numerical results and discussion. Conclusions and perspectives for future work are provided in Section 6.

## 2. Reynolds-Averaged Navier–Stokes equations and turbulence models

The incompressible RANS equations read:

$$\frac{\partial \bar{u}_i}{\partial x_i} = 0 \quad (1)$$

$$\frac{\partial \bar{u}_i}{\partial t} + \frac{\partial (\bar{u}_i \bar{u}_j)}{\partial x_j} = -\frac{1}{\rho} \frac{\partial \bar{p}}{\partial x_i} + \frac{\partial}{\partial x_j} \left( \nu \frac{\partial \bar{u}_i}{\partial x_j} - \overline{u'_i u'_j} \right), \quad (2)$$

where  $\rho$  is the constant density,  $\nu$  the fluid kinematic viscosity,  $\bar{u}_i$  and  $\bar{p}$  the averaged velocity components and pressure and  $u'_i$  the velocity fluctuations.

The unclosed term  $\tau_{ij} = \overline{u'_i u'_j}$  is the kinematic Reynolds stress tensor. It can be decomposed into an isotropic part  $\frac{2}{3}k\delta_{ij}$  and an anisotropic part  $a_{ij} = 2kb_{ij}$  (with  $b_{ij}$  a non-dimensional anisotropy tensor), such that:

$$\tau_{ij} = \overline{u'_i u'_j} = 2k(b_{ij} + \frac{1}{3}\delta_{ij}), \quad (3)$$

where  $k = tr(\tau_{ij})/2$  is the turbulent kinetic energy. Therefore, the modeling of the entire range of turbulent scales in the RANS approach reduces to the modeling of  $k$  and of the anisotropy tensor. This is generally done by introducing a constitutive relation for  $b_{ij}$ , i.e. a functional form relating its components to the mean field.

### 2.1. Boussinesq analogy and LEVM models

Most turbulence models currently used in industrial codes are LEVM. Such models rely on the so-called Boussinesq analogy, whereby the anisotropic part of  $\tau_{ij}$  is written as a linear function of the mean rate-of-strain  $S_{ij} = \frac{1}{2} \left( \frac{\partial \bar{u}_i}{\partial x_j} + \frac{\partial \bar{u}_j}{\partial x_i} \right)$ :

$$b_{ij} = -\frac{\nu_t}{k} S_{ij} \quad (4)$$

with  $\nu_t$  the eddy viscosity coefficient.

The LEVM constitutive relation 4 is then closed by expressing  $\nu_t$  as a function of the mean flow. Most often,  $\nu_t$  is computed using a transport-equation model such as the  $k-\omega$  SST [22], used here as the baseline model. For completeness, the SST  $k-\omega$  equations are recalled in Appendix A. Although this model is believed to be one of the most accurate LEVM models on average, it still shows limitations in providing reliable results for flows with separation, streamline curvature or strong pressure gradients [2, 3].

## 2.2. Augmented Boussinesq analogy and EARSM models

To overcome the limitations of LEVM models, more sophisticated approaches have been developed, such as the generalized eddy viscosity models [7]. In particular, EARSM generalize the linear eddy viscosity concept by assuming that the anisotropy of the Reynolds-stress depends not only on the strain rate tensor  $S_{ij}$  but also on the rotation rate tensor  $\Omega_{ij} = \frac{1}{2} \left( \frac{\partial \bar{u}_i}{\partial x_j} - \frac{\partial \bar{u}_j}{\partial x_i} \right)$  through a non linear relationship.

Such models can be constructed from a baseline LEVM using the so-called augmented Boussinesq analogy:

$$\tau_{ij} = 2k(b_{ij} + \frac{1}{3}\delta_{ij}), \quad (5)$$

where  $b_{ij} = b_{ij}^{bl} + b_{ij}^{\Delta}$  with  $b_{ij}^{bl} = -\frac{\nu_t}{k} S_{ij}$  and  $b_{ij}^{\Delta}$  is the extra anisotropy tensor, used to correct the baseline Boussinesq model  $b_{ij}^{bl}$ .

Following this approach, an EARSM can be constructed by specifying a non linear relationship between the extra anisotropy tensor  $b_{ij}^{\Delta}$  and the strain rate tensor and the rotation rate tensor. Following [7], the most general form of the anisotropic Reynolds-stress correction is derived via the Cayley-Hamilton theorem:

$$b_{ij}^{\Delta}(S_{ij}, \Omega_{ij}) = \sum_{\lambda=1}^{10} G_{\lambda}(I_1, \dots, I_5) T_{ij}^{(\lambda)}, \quad (6)$$

using a minimal integrity basis of ten tensors  $T_{ij}^{(\lambda)}$  and five invariants  $I_m$ , written as functions of the non-dimensional mean strain rate  $\hat{S}_{ij} = \frac{1}{2\omega} \left( \frac{\partial \bar{u}_i}{\partial x_j} + \frac{\partial \bar{u}_j}{\partial x_i} \right)$  and rotation rate  $\hat{\Omega}_{ij} = \frac{1}{2\omega} \left( \frac{\partial \bar{u}_i}{\partial x_j} - \frac{\partial \bar{u}_j}{\partial x_i} \right)$ . In the following, we focus on two-dimensional flow cases, for which the first three base tensors form a linearly independent basis and only the first two invariants are nonzero [7], and the set of base tensors and invariants reads

$$\begin{aligned} T_{ij}^{(1)} &= \hat{S}_{ij}, \quad T_{ij}^{(2)} = \hat{S}_{ik}\hat{\Omega}_{kj} - \hat{\Omega}_{ik}\hat{S}_{kj}, \\ T_{ij}^{(3)} &= \hat{S}_{ik}\hat{S}_{kj} - \frac{1}{3}\delta_{ij}\hat{S}_{mn}\hat{S}_{nm} \\ I_1 &= \hat{S}_{mn}\hat{S}_{nm}, \quad I_2 = \hat{\Omega}_{mn}\hat{\Omega}_{nm}. \end{aligned}$$

Deriving EARSM models then consists in finding a set of scalar functions  $G_{\lambda}$ , which are classically obtained from physical considerations [7, 8]. In the following, we present a deterministic symbolic identification method to build EARSM models from high-fidelity data sets, cast in the form of equations (5) and (6).

In the numerical experiments of section 5, we also consider a general purpose EARSM, recently proposed in [23] and referred-to as BSL-EARSM, for comparison with customized data-driven models. Its formulation is briefly recalled in Appendix B.

### 2.3. CFD solver

The CFD-SpaRTA methodology requires the implementation of the general formulation of the augmented EARSM in a CFD solver. In the present work, the open-source finite-volume code OpenFOAM [24] has been used. The RANS equation system (equations 1 and 2) are solved using the SIMPLE algorithm [25]; the convective terms are discretized using linear upwinding and viscous terms with 2nd order central differencing. The solution is advanced to the steady state using a Gauss-Seidel smoother.

## 3. Flow configurations and data sets

The aim of the present work being the development of data-driven corrections to turbulence models, all numerical experiments are carried out for a family of flow configurations that challenge standard RANS models, and specifically LEVM. In particular, we have considered the same cases reported in [1], representing flows in 2D channels with variable cross sections. High fidelity data from DNS or well-resolved LES are available for model training and validation. To ensure that discretization errors remain low with respect to turbulence modeling errors, the RANS simulation use sufficiently fine meshes.

More details of the flow configurations and data sets used in the present numerical experiments presented are given below.

### 3.1. Periodic hill flow ( $PH_{10595}$ )

The so-called periodic hill flow consists of a flow through a channel constrained by periodic restrictions (hills) of height  $h$ . For a channel segment comprised between two adjacent hills, the flow separates on the lee-side of the first hill and reattaches between the hills. The test case has been widely investigated in the literature, both experimentally and numerically. The high-fidelity LES data used in the present work are from [26] for  $Re = 10595$  ( $PH_{10595}$ ), where  $Re$  is a Reynolds number based on the bulk velocity in the restricted section and the hill height. Our RANS simulations use a computational grid consisting of  $120 \times 130$  cells. Cyclic boundary conditions are used at the inlet and outlet and a forcing term is applied to maintain a constant flow rate through the channel.

### 3.2. Converging-diverging channel at $Re=12600$ ( $CD_{12600}$ )

This configuration corresponds to a 2D channel of half-height  $H$  with an asymmetric bump of height  $h \approx 2/3H$  located on the bottom wall. The Reynolds number (based on the channel half-height and inlet conditions) is  $Re = 12600$ . A small separation occurs on the lee-side of the bump. For this test case, high-fidelity DNS data from [27] are available. The RANS simulations are based on a mesh of  $140 \times 100$  cells. A velocity profile obtained from a companion channel-flow simulation is imposed at the inlet of the computational domain.

### 3.3. Curved backward-facing step (CBFS<sub>13700</sub>)

The case consists in a 2D flow over a gently-curved backward-facing step of height  $h$ , producing a separation bubble. The upstream channel height is  $8.52h$  and the Reynolds number, based on the inlet velocity and step height, is 13700. High-fidelity LES data from [28] are used for training. For the RANS simulations, the mesh consists of 140 x 150 cells. Slip conditions are used at the upper boundary, and a velocity profile obtained from a fully-developed boundary layer simulation is set at the domain inlet.

## 4. Symbolic identification methodology

In this section, we introduce the general form of candidate models, constructed from a library of functions. Then we recall the CFD-free SpaRTA training algorithm of [1]. Finally, we describe in detail the steps of the new CFD-driven symbolic identification algorithm.

### 4.1. Symbolic identification of EARSM

Following the approach proposed in [1], the scalar functions  $G_\lambda$  are approximated as linear combinations of candidate functions of  $I_1$  and  $I_2$ , consisting of monomials up to order 6:

$$\mathbf{B} = [c, I_1, I_2, I_1^2, I_1 I_2, I_2^2, I_1^3, I_1^2 I_2, I_1 I_2^2, I_2^3, I_1^4, I_1^3 I_2, I_1^2 I_2^2, I_1 I_2^3, I_2^4, I_1^5, I_1^4 I_2, I_1^3 I_2^2, I_1^2 I_2^3, I_1 I_2^4, I_2^5, I_1^6, I_1^5 I_2, I_1^4 I_2^2, I_1^3 I_2^3, I_1^2 I_2^4, I_1 I_2^5, I_2^6]^T. \quad (7)$$

Given this library, the full expression of eq. (6) becomes:

$$\begin{aligned} b_{ij}^\Delta(S_{ij}, \Omega_{ij}) &= \theta_0^{b_{ij}^\Delta} T_{ij}^{(1)} + \theta_1^{b_{ij}^\Delta} I_1 T_{ij}^{(1)} + \theta_2^{b_{ij}^\Delta} I_2 T_{ij}^{(1)} + \dots \\ &+ \theta_{26}^{b_{ij}^\Delta} I_1 I_2^5 T_{ij}^{(1)} + \theta_{27}^{b_{ij}^\Delta} I_2^6 T_{ij}^{(1)} \\ &+ \theta_{28}^{b_{ij}^\Delta} T_{ij}^{(2)} + \theta_{29}^{b_{ij}^\Delta} I_1 T_{ij}^{(2)} + \theta_{30}^{b_{ij}^\Delta} I_2 T_{ij}^{(2)} + \dots \\ &+ \theta_{54}^{b_{ij}^\Delta} I_1 I_2^5 T_{ij}^{(2)} + \theta_{55}^{b_{ij}^\Delta} I_2^6 T_{ij}^{(2)} \\ &+ \theta_{56}^{b_{ij}^\Delta} T_{ij}^{(3)} + \theta_{57}^{b_{ij}^\Delta} I_1 T_{ij}^{(3)} + \theta_{58}^{b_{ij}^\Delta} I_2 T_{ij}^{(3)} + \dots \\ &+ \theta_{82}^{b_{ij}^\Delta} I_1 I_2^5 T_{ij}^{(3)} + \theta_{83}^{b_{ij}^\Delta} I_2^6 T_{ij}^{(3)}, \end{aligned} \quad (8)$$

where the vector of coefficients:

$$\Theta^{b_{ij}^\Delta} = [\theta_0^{b_{ij}^\Delta}, \theta_1^{b_{ij}^\Delta}, \theta_2^{b_{ij}^\Delta}, \dots, \theta_{83}^{b_{ij}^\Delta}]^T \in \mathbb{R}^{84} \quad (9)$$

has to be determined.

A major improvement proposed in [1] consists in the introduction of a corrective term in the turbulent transport equations, in addition to the use of the generalized eddy viscosity formulation. Specifically, a residual term  $R$  is added to the model transport equations and the augmented k- $\omega$ -SST model becomes:

$$\frac{\partial k}{\partial t} + \bar{u}_j \frac{\partial k}{\partial x_j} = P_k + R - \beta^* k \omega + \frac{\partial}{\partial x_j} [(\nu + \sigma_k \nu_t) \frac{\partial k}{\partial x_j}] \quad (10)$$

$$\frac{\partial \omega}{\partial t} + \bar{u}_j \frac{\partial \omega}{\partial x_j} = \frac{\gamma}{\nu_t} (P_k + R) - \beta \omega^2 + \frac{\partial}{\partial x_j} [(\nu + \sigma_\omega \nu_t) \frac{\partial \omega}{\partial x_j}] + CD_{k\omega}, \quad (11)$$

with  $P_k = \min(-2k(b_{ij}^{bl} + b_{ij}^\Delta) \partial_j U_i, 10\beta^* \omega k)$ .

The residual  $R$  can be positive or negative and it represents a correction of the model production term. Introducing a suitable non-dimensional correction tensor  $b_{ij}^R$ , the model for  $R$  writes:

$$R = 2kb_{ij}^R \frac{\partial \bar{u}_j}{\partial x_i}, \quad (12)$$

where  $b_{ij}^R$  is also decomposed according to the Cayley-Hamilton theorem:

$$\begin{aligned} b_{ij}^R(S_{ij}, \Omega_{ij}) &= \theta_0^R T_{ij}^{(1)} + \theta_1^R I_1 T_{ij}^{(1)} + \theta_2^R I_2 T_{ij}^{(1)} + \dots \\ &+ \theta_{26}^R I_1 I_2^5 T_{ij}^{(1)} + \theta_{27}^R I_2^6 T_{ij}^{(1)} \\ &+ \theta_{28}^R T_{ij}^{(2)} + \theta_{29}^R I_1 T_{ij}^{(2)} + \theta_{30}^R I_2 T_{ij}^{(2)} + \dots \\ &+ \theta_{54}^R I_1 I_2^5 T_{ij}^{(2)} + \theta_{55}^R I_2^6 T_{ij}^{(2)} \\ &+ \theta_{56}^R T_{ij}^{(3)} + \theta_{57}^R I_1 T_{ij}^{(3)} + \theta_{58}^R I_2 T_{ij}^{(3)} + \dots \\ &+ \theta_{82}^R I_1 I_2^5 T_{ij}^{(3)} + \theta_{83}^R I_2^6 T_{ij}^{(3)}, \end{aligned} \quad (13)$$

The vector of coefficients:

$$\Theta^R = [\theta_0^R, \theta_1^R, \theta_2^R, \dots, \theta_{83}^R]^T \in \mathbb{R}^{84} \quad (14)$$

needs to be determined alongside with  $\Theta^{b_{ij}^\Delta}$ .

Once the general library of candidate models has been chosen, the difference between the CFD-free and the CFD-driven approaches relies in the method used to determine  $\Theta^{b_{ij}^\Delta}$  and  $\Theta^R$ .

#### 4.2. CFD-free SpARTA algorithm

In the CFD-free approach, high fidelity data for the velocity field,  $\bar{u}_i^*$ , turbulent kinetic energy  $k^*$  and Reynolds-stresses  $\tau_{ij}^*$  are used to train the model. Such data are pre-processed prior to use for model learning.

The high-fidelity anisotropy tensor  $b_{ij}^*$  is obtained from equation (5). The next step of the method is the determination of the high fidelity values for  $b_{ij}^\Delta$  and  $R$ . Knowing  $b_{ij}^*$ ,  $b_{ij}^{\Delta,*} = b_{ij}^* + \frac{\nu_i^*}{k^*} S_{ij}^*$  is directly derived if a high-fidelity ansatz of the turbulent viscosity  $\nu_i^*$  is provided. The latter can be computed using the relation (A.3), setting  $k = k^*$ . However, a high fidelity value of  $\omega$  is also needed. For this purpose, a so-called  $k$ -corrective-frozen-RANS algorithm is used, whereby a high-fidelity estimate of the residual  $R^*$  is computed alongside  $\omega^*$ . This process consists in injecting  $\bar{u}_i^*$ ,  $k^*$  and  $b_{ij}^*$  in equations (10) and (11) and iteratively computing  $\omega^*$  by solving equation (11). At each iteration,  $R^*$  is computed as the residual of equation (10) and fed back into equation (11). On

completion of the preceding manipulations, high fidelity fields for  $b_{ij}^{\Delta,*}$  and  $R^*$  are available.

High-fidelity counterparts of the terms in the library  $\mathbf{B}^*$  are computed from the high-fidelity velocity field by using relations (7); similarly, high-fidelity estimates of the basis tensors  $T_{ij}^{(\lambda,*)}$  are computed.  $\mathbf{B}^*$  and  $T_{ij}^{(\lambda,*)}$  are then used to compute the  $b_{ij}^{\Delta}$  and  $R$  fields corresponding to candidate models defined by specifying the sets of coefficients  $\Theta^{b_{ij}^{\Delta}}$  and  $\Theta^R$ . For each field  $\Delta$  ( $\Delta$  indicating either  $b_{ij}^{\Delta}$  or  $R$ ) the following optimization problem can be constructed:

$$\Theta = \underset{\hat{\Theta}}{\operatorname{argmin}} \|\Delta^* - \Delta(\hat{\Theta})\|_2^2 + \text{regularization terms}, \quad (15)$$

where  $\|\bullet\|_2$  stands for the  $l_2$  norm of the error,  $\hat{\Theta}$  is the vector  $\Theta^{b_{ij}^{\Delta}}$  (respectively  $\Theta^R$ ) if  $\Delta$  represents  $b_{ij}^{\Delta}$  (respectively  $R$ ).  $\Delta^*$  is the high fidelity value of the field and  $\Delta(\hat{\Theta})$  is the field reconstructed using the model corresponding to  $\hat{\Theta}$ .

The choice of the regularization terms is crucial to efficiently select a small subset of relevant terms among those constituting the highly dimensional symbolic library. The goal of the whole methodology being the construction of augmented RANS models optimized for a specific class of flows, the learnt model should be general enough to be effective for the simulation of flows belonging to the same class (e.g. flows with separations). Without the regularization terms, the problem formulated by equation (15) reduces to a standard mean-squares optimization problem whose resolution leads to dense coefficient vectors  $\Theta^{b_{ij}^{\Delta}}$  and  $\Theta^R$ , possibly overfitting the data. In [1], this effect is mitigated by using an elastic net regularization, known to be sparsity promoting [29, 30] :

$$\text{regularization terms} = \lambda \rho \|\hat{\Theta}\|_1 + 0.5 \lambda (1 - \rho) \|\hat{\Theta}\|_2^2, \quad (16)$$

where  $\rho \in [0, 1]$  is the blending parameter between the  $l_1$ - and  $l_2$ - norm regularization and  $\lambda$  is the regularization weight. The blending parameter  $\rho$  relaxes the  $l_1$ - regularization, that tends to select only one function in sets of correlated functions and therefore degrade the predictive performance of the inferred models. This relaxation allows to find sparse models with good predictive performance. The regularization weight  $\lambda$  also controls the sparsity of the inferred models (independently of  $\rho$ ). As the optimal value of  $(\rho, \lambda)$  is not known a priori, the optimization problem given in equation (15) must be solved for a grid of pairs  $(\rho_{1 \leq i \leq N}, \lambda_{1 \leq j \leq M})$ . The optimal pair  $(\rho, \lambda)$  is evaluated a posteriori through cross validation [31] over a set of test flows different from the training one, for which high fidelity data are available. Models learned from the high-fidelity dataset for one flow case are tested on the remaining cases. For each case, a single model is chosen as the best-performing one. These models can then be used as a predictive tool for the simulation of other test cases not included in training or validation sets.

### 4.3. CFD-driven symbolic identification

The technical flow diagram of the CFD-driven algorithm that we have developed in the present work to determine  $\Theta^{b_{ij}^{\Delta}}$  and  $\Theta^R$  is sketched in figure

1.

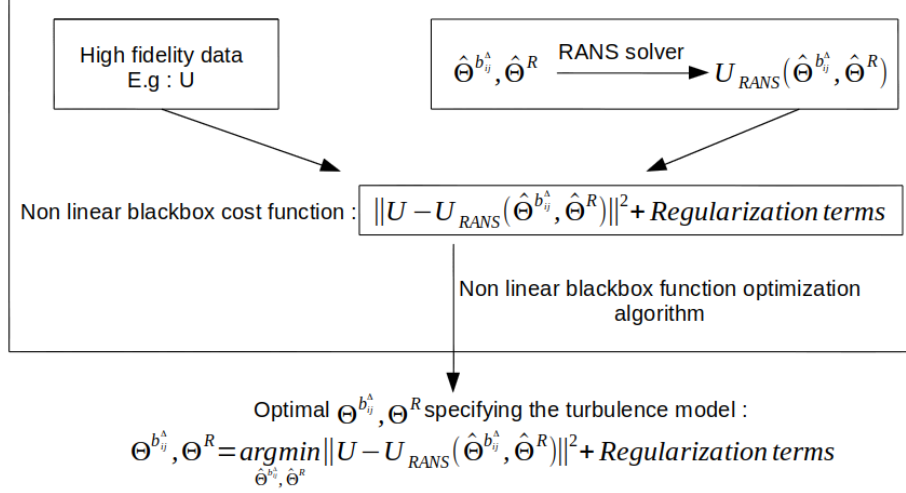


Figure 1: Technical flow diagram of the CFD-driven SpaRTA method.  $U$  represents any quantity of interest considered as the target for model training.

The first step of the method consists in gathering high fidelity data for a flow or a class of flows for which we want to improve the accuracy of the baseline model. It should be emphasized that, while the CFD-free approach requires data for second-order quantities like  $k$  and  $\tau_{ij}$ , observations available for any quantity of interest (velocity or pressure measurements, global aerodynamic coefficients, etc.) can be used as a target for training. In the flowchart of figure 1, we assumed that high fidelity data are available for a quantity of interest  $U$ : this could be, for instance, the streamwise velocity component  $\bar{u}_1$  but the same procedure applies for any other data set. Typically,  $U$  is a vector of high-fidelity samples extracted at selected locations in the flow field and concatenated into a single vector.

As a second step, we implement the general form of the augmented turbulence model in the CFD-solver, here OpenFOAM [24]. The latter is used to evaluate the quantity  $U$  using a candidate augmented turbulence model specified by any instance of the vectors  $\hat{\Theta}^{b_{ij}^\Delta}$  and  $\hat{\Theta}^R$ . The output RANS data for  $U$  are indicated as  $U_{RANS}(\hat{\Theta}^{b_{ij}^\Delta}, \hat{\Theta}^R)$ . Then, the fitness of candidate models is evaluated in terms of the mean squared error  $\|U^* - U_{RANS}(\hat{\Theta}^{b_{ij}^\Delta}, \hat{\Theta}^R)\|_2^2$  between the high fidelity data  $U^*$  and the RANS model prediction  $U_{RANS}(\hat{\Theta}^{b_{ij}^\Delta}, \hat{\Theta}^R)$ . The model can then be constructed by solving the following optimization problem:

$$(\Theta^{b_{ij}^\Delta}, \Theta^R) = \underset{(\hat{\Theta}^{b_{ij}^\Delta}, \hat{\Theta}^R)}{\operatorname{argmin}} \|U - U_{RANS}(\hat{\Theta}^{b_{ij}^\Delta}, \hat{\Theta}^R)\|_2^2 + \text{regularization terms}, \quad (17)$$

where regularization terms are added to the least squares formulation to prevent overfitting of the high fidelity data. The choice of the regularization is discussed in the following.

The preceding cost function is a non-linear black-box function involving a RANS simulation for any choice of  $\hat{\Theta}^{b^\Delta}$ ,  $\hat{\Theta}^R$ , and is therefore costly in terms of CPU time. In the following, problem 17 is optimized using the Constrained Optimization using Response Surface (CORS) algorithm [21], which uses the response surface methodology to approximate the expensive function using a limited number of function evaluations. The optimization is subsequently performed on this response surface. Hereafter we use the implementation of the CORS algorithm available in the *blackbox* python module [32]. A short description of the algorithm is given in Appendix C.

Given the difficulty of constructing accurate response surfaces in highly dimensional parameter spaces (here,  $D = 168$ ), a preliminary local sensitivity analysis is conducted to identify the most influential parameters and reduce the search space. Afterwards, search ranges for model parameters are assigned by prescribing Reynolds-stress realizability conditions. Finally, the regularization terms in the fitness function definition (17) are specified. These three steps are described into more details in the following.

#### 4.3.1. Local sensitivity analysis

In the CORS algorithm, the number of cost function evaluations  $N$  allowed during the optimization process is fixed a priori. It is subjected to the constraint  $N > 2D$ , where  $D$  is the dimensionality of the parameter space. As the general formulation of the augmented model involves 168 coefficients, we have at least  $N = 336$ . This number of evaluations is relatively high, implying a considerable numerical cost of the training procedure. Additionally, for highly dimensional spaces, the response surface may not provide an accurate enough approximation of the true cost function.

To reduce the size of the parameter space, we carry out a local sensitivity analysis around the baseline model formulation (corresponding to  $\theta^{b^\Delta} = 0$  and  $\theta^R = 0$ ) to determine the most influential model coefficients. For that purpose, a small perturbation ( $O(10^{-3})$ ) is successively added to each parameter, and the derivatives of the cost functions with respect to the coefficients are computed using one-sided finite differences.

The results of the sensitivity study are reported in the following for the 2D periodic hills test case at  $Re = 10595$  (PH<sub>10595</sub>) using the high-fidelity data from [26]. The cost function is based on high fidelity velocity and Reynolds stress profiles at abscissas  $x = (0.05, 0.5, 1.0, 2.0, 3.0, 4.0, 5.0, 6.0, 7.0, 8.0)$ . Figure 2 reports sensitivity derivatives of the cost function with respect to the parameters of the  $b^\Delta$  model. The abscissa correspond to parameter subscripts. Parameters with subscripts 0 to 27, 28-55 and 56-83 appear in the function coefficients of  $T_{ij}^{(1)}$ ,  $T_{ij}^{(2)}$  and  $T_{ij}^{(3)}$ , respectively. Several comments are in order. First, parameters associated with the first tensor (corresponding to a correction of the linear eddy viscosity coefficient) are overall more influential than with the

others. Parameters involved in the quadratic tensorial terms play the role of a higher-order correction to the constitutive law. Second, the sensitivity to the parameters decays rapidly with the degree of the monomial functions, and terms up to the second degree are at least one order of magnitude larger than the coefficients of the higher order terms. For this reason, only monomials up to the second order are retained in the library of candidate functions (equation (7)). Similar results are found for the parameters in  $b^R$ . With the preceding parameter selection, the number of coefficients to be determined is then reduced to 36 instead of 168.

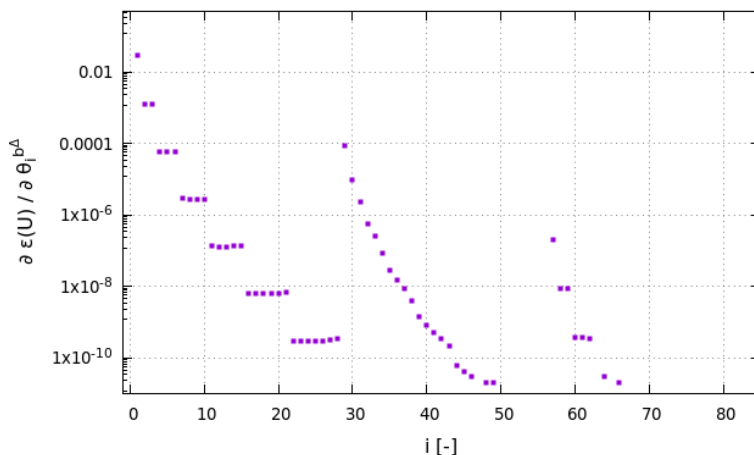


Figure 2: Sensitivity derivatives of the cost function (based on the velocity components for case PH<sub>10595</sub>) to the parameters  $\theta^{b^\Delta}$ .

#### 4.3.2. Selection of parameter ranges

The initial range of each model coefficient must be specified prior to the CORS optimization. For each  $\Theta_{1 \leq i \leq 36}$  of  $\Theta^{b_{ij}^\Delta}$  and  $\Theta^R$ , the search space is set as:

$$a_i \leq \Theta_i \leq b_i \quad (18)$$

where  $a_i \in \mathbb{R}$  and  $b_i \in \mathbb{R}$  are respectively the lower and upper bound of the range of variation of candidate model coefficients. In our setup of the CFD-driven method, the coefficients ranges are set by enforcing realizability conditions for the Reynolds stress tensor [33].

For that purpose, a realizability study is performed using the Reynolds stress anisotropy barycentric map representation [20, 34, 35]. The modeled anisotropy tensor is initially computed from high fidelity data with each parameter  $\Theta^{b_{ij}^\Delta}$  varying in the range  $[-7, 7]$ . The tensor eigenvalues are noted  $\lambda_1$ ,  $\lambda_2$  and  $\lambda_3$  (with  $\lambda_1 \geq \lambda_2 \geq \lambda_3$ ). Following [20], we construct an equilateral triangle defined by the three corners  $\mathbf{x}_{1C}$ ,  $\mathbf{x}_{2C}$  and  $\mathbf{x}_{3C}$ , where  $\mathbf{x} = (x, y)$  is a position vector. The three corners the triangle represent the three limiting physical

states of turbulence. We then construct the following linear mapping between the anisotropy eigenvalues and the coordinates  $x$  :

$$\mathbf{x} = \mathbf{x}_{1C}(\lambda_1 - \lambda_2) + \mathbf{x}_{2C}(2\lambda_2 - 2\lambda_3) + \mathbf{x}_{3C}(3\lambda_3 + 1). \quad (19)$$

As any realizable state of turbulence is a convex combination of the three limiting states of turbulence,  $\mathbf{x}$  must lie within the triangle if  $\lambda_1$ ,  $\lambda_2$  and  $\lambda_3$  correspond to a realizable anisotropy tensor. For a given set of coefficients  $\Theta^{b_{ij}^\Delta}$ , the eigenvalues of  $b_{ij}$  can be computed for each mesh point and the corresponding  $\mathbf{x}$  can be placed in the barycentric map in order to verify if the resulting anisotropy tensor field corresponds to a physically realizable flow.

A total of 50000 vectors  $\Theta^{b_{ij}^\Delta}$  are generated using uniform Latin Hypercube sampling. For each sample, the corresponding anisotropy tensor eigenvalues are plotted in the barycentric map coordinate system for each mesh point. Sets of parameters leading to a violation of the realizability condition are then discarded. For the remaining sets of parameters, we compute the average value, the standard deviation and the minimum and maximum values taken by each component of  $\Theta^{b_{ij}^\Delta}$ . Realizable values of the coefficients are equal to 0 in the mean, with a variance of approximately 4. Therefore, ranges  $[-2, 2]$  are finally adopted for each  $\Theta^{b_{ij}^\Delta}$ . The same search ranges are applied to the coefficients in  $\Theta^R$ .

In figure 3a, the modeled anisotropy tensor at each mesh cell has been placed in the barycentric map for 100 random vectors  $\Theta^{b_{ij}^\Delta}$  sampled using uniform Latin Hypercube sampling in range  $[-7, 7]^{84}$ . The figure shows that the anisotropy tensor is not realizable for a large fraction of mesh points. In figure 3b, the sampling has been performed in range  $[-2, 2]^{84}$ . The fraction of mesh points possibly corresponding to non realizable anisotropy tensors is drastically reduced. Therefore, an initial parameter range in  $[-2, 2]$  as the search space for each  $\Theta^{b_{ij}^\Delta}$  ensures that most candidate models evaluated in the optimization loop lead to realizable anisotropy tensor fields throughout the computational domain.

#### 4.3.3. Regularization terms

The regularization terms of the optimization problem (17) have to be specified. Unlike the CFD-free SpaRTA, the CFD-driven training involves a non-linear dependency of the cost function on the model parameters, due to the nonlinearity of the RANS equations. Sparsity-promoting regularization of non-linear parameters would require an approximate computation of the cost function derivatives with respect to the parameters or function linearization [36, 37]. This can be efficiently done for CFD using an adjoint solver, which is not always promptly available. For this reason, we choose to simply add an elastic-net regularization as in the CFD-SpaRTA, and we examine its effect on the complexity and generalizability of the resulting models. The optimization problem of equation 17 is reformulated as:

$$\Theta = \underset{\hat{\Theta}}{\operatorname{argmin}} \|U - U_{RANS}(\hat{\Theta})\|_2^2 + \lambda\rho\|\hat{\Theta}\|_1 + 0.5\lambda(1 - \rho)\|\hat{\Theta}\|_2^2, \quad (20)$$

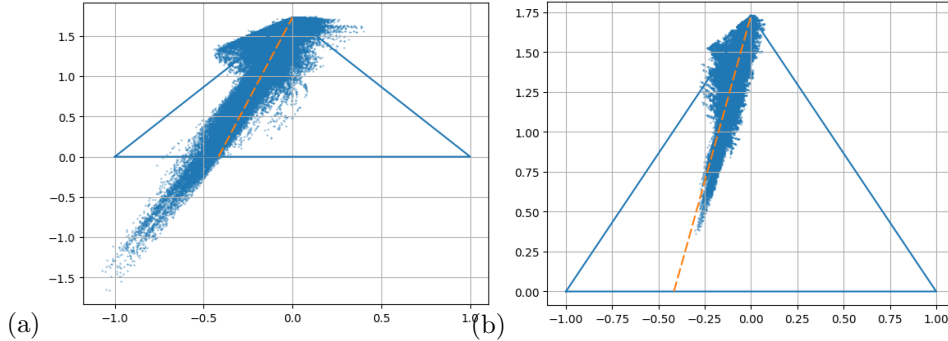


Figure 3: Modeled anisotropy tensor at each mesh cell placed in the barycentric map for 100 random vectors  $\Theta^{b_{ij}^{\Delta}}$  sampled using uniform Latin Hypercube sampling. (a) sampling in range  $[-7, 7]^{84}$ . (b) Sampling in range  $[-2, 2]^{84}$ .

where  $\rho \in [0, 1]$  is the blending parameter between the  $l_1$ - and  $l_2$ - norm regularization and  $\lambda$  is the regularization weight. As the optimal value of  $(\rho, \lambda)$  is not known a priori, the optimization problem given in equation 20 must be solved for a grid of pairs  $(\rho_{1 \leq i \leq N}, \lambda_{1 \leq j \leq M})$  for a set of flows for which high fidelity data are available. In the aim of reducing the total number of optimization runs, we select a 1D net, with  $\rho = 0.5$  and  $\lambda = 10^{-2}, 10^{-3}, 10^{-4}, 10^{-5}, 10^{-6}, 10^{-7}$ .

In the following, optimization runs are carried out for all six points of the net, resulting in six alternative models for each test case of section 3. Cross-validation [31] is then used to select the best-performing model across all test data sets. The performance of each candidate is arbitrarily evaluated as the mean squared error with respect to the high fidelity data. Other choices are possible.

## 5. Numerical results

### 5.1. Model discovery

In the following, the CFD-driven SpARtA is applied to the flow configurations of Section 3. Two series of numerical experiments are carried out, using different training data.

In a first series of experiments, high-fidelity data for the Reynolds stresses are used to train the model, as in the CFD-free SpARtA algorithm. However, in this case no additional data for the velocity field or the transported turbulent quantities is needed and the  $k$ -corrective frozen-RANS procedure is not applied. More precisely, the training data are vertical profiles of  $\tau_{11}$ ,  $\tau_{22}$  and  $\tau_{12}$ . Profiles at  $x/h = (0.05, 0.5, 1.0, 2.0, 3.0, 4.0, 5.0, 6.0, 7.0, 8.0)$  are used for the PH<sub>10595</sub> case; for the CD<sub>12600</sub> we use profiles at  $x/H = (5.5, 6.5, 7.5, 8.5, 9.5, 10.5, 11.5, 12)$ ; finally, the profiles at  $x = (0.1, 1.5, 3.0, 4.5, 6.0, 7.5)$  are considered for case CBFS<sub>13700</sub>. The amount of data used for the training is very sparse compared to the number of degrees of freedom used to solve the CFD problem: they

represent 8.3%, 5.7% and 4.28% of the total number of mesh points, used respectively for  $\text{PH}_{10595}$ ,  $\text{CD}_{12600}$  and  $\text{CBFS}_{13700}$ . The blending parameter of the elastic net regularization term is fixed to  $\rho = 0.5$  and six values of the LASSO regularization parameter are considered, as discussed previously. For each net point, the CORS algorithm has been run using a number of cost function evaluations  $N = 78$ , close to the minimum recommended value. Coefficients below a threshold of 0.1 are set to zero, and we verified numerically that this has a negligible influence on the solution. The model training step leads to the discovery of  $3 \times 6$  alternative models that are submitted to cross-validation: models trained for a flow configuration are applied to the two other cases. A total of 1458 RANS simulations have therefore been performed for the model discovery and the cross-validation, corresponding to approximately 4500 core-hours on a standard workstation. The learning process is obviously much more expensive than the CFD-free procedure but it remains affordable without use of intensive computational facilities. Cross-validation errors are reported in figure 4, normalized by the mean-squared error of the baseline  $k-\omega$  SST model. Most models show an improvement over the baseline. Models trained on  $\text{CD}_{12600}$  produce higher errors than the other ones, unless low values of  $\lambda$  are used. Of note, models with low  $\lambda$  generalize well throughout the test set.

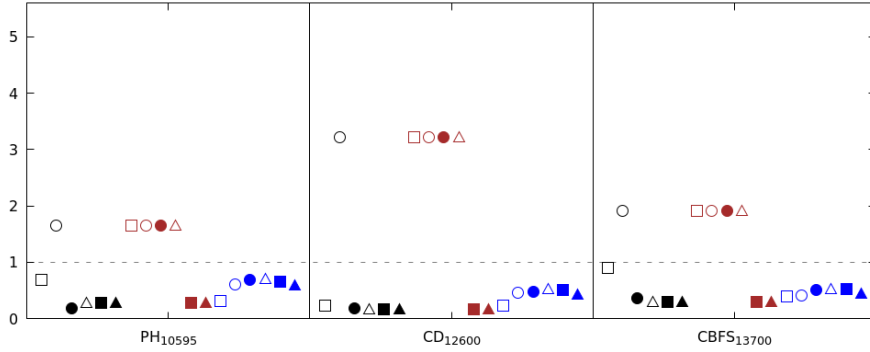


Figure 4: Cross-validation errors based on velocity profiles  $(\overline{u_1}, \overline{u_2})$  for models trained on Reynolds-stress data. The errors are normalized with the mean-squared error of the baseline  $k-\omega$  SST model. Black : models trained on  $\text{PH}_{10595}$ . Red : models trained on  $\text{CD}_{12600}$ . Blue : models trained on  $\text{CBFS}_{13700}$ . □ :  $\lambda = 10^{-2}$ . ○ :  $\lambda = 10^{-3}$ . ● :  $\lambda = 10^{-4}$ . △ :  $\lambda = 10^{-5}$ . ■ :  $\lambda = 10^{-6}$ . ▲ :  $\lambda = 10^{-7}$ .

The best-performing model is identified as the one with the lower average error across the three test cases. This model, trained on  $\text{PH}_{10595}$  with  $\lambda = 10^{-4}$ , is named  $M^{(\tau, PH, \lambda=10^{-4})}$  in the following. The mathematical expressions for the two correction tensors involve 30 out of the 36 candidate functions left after

parameter space reduction:

$$\begin{aligned}
 b_{ij}^{\Delta} = & -(0.71337 + 0.56749I_1 + 0.57197I_2 + 0.21847I_1I_2 + 1.6645I_2^2)T_{ij}^{(1)} \\
 & -(0.5365 + 1.0711I_1 + 1.0149I_2 + 1.2724I_1^2 + 1.8565I_2^2)T_{ij}^{(2)} \\
 & -(1.4817 + 1.8107I_1 + 0.35296I_2 + 0.45661I_1^2 + 0.41543I_1I_2)T_{ij}^{(3)}
 \end{aligned} \tag{21}$$

$$\begin{aligned}
 b_{ij}^R = & -(0.51331 + 0.26013I_1 + 0.59803I_2 + 0.45579I_2^2)T_{ij}^{(1)} \\
 & -(0.54786 + 1.136I_1 + 1.7713I_2 + 0.83876I_1^2 + 0.18759I_1I_2 + 1.5662I_2^2)T_{ij}^{(2)} \\
 & -(1.6974 + 1.4721I_1 + 0.31389I_1^2 + 0.81017I_1I_2 + 0.59936I_2^2)T_{ij}^{(3)}
 \end{aligned} \tag{22}$$

In the second series of experiments, the method is trained against high fidelity velocity profiles and skin friction data to test its ability to discover models optimized for any target quantity of interest and to assess the sensitivity of the symbolic identification procedure to the kind of training data. Velocity profiles ( $\overline{u}_1$  and  $\overline{u}_2$ ) are extracted at the same locations as Reynolds stress profiles, and the skin friction data are extracted along the bottom walls in all cases. In this setting the data represent 9.1%, 6.7% and 4.95% of the total number of mesh points for PH<sub>10595</sub>, CD<sub>12600</sub> and CBFS<sub>13700</sub>, respectively. Cross validation errors for the 18 discovered models are reported in figure 5. In this case, the test errors are lower, since the testing variable (the longitudinal velocity) is also used for training.

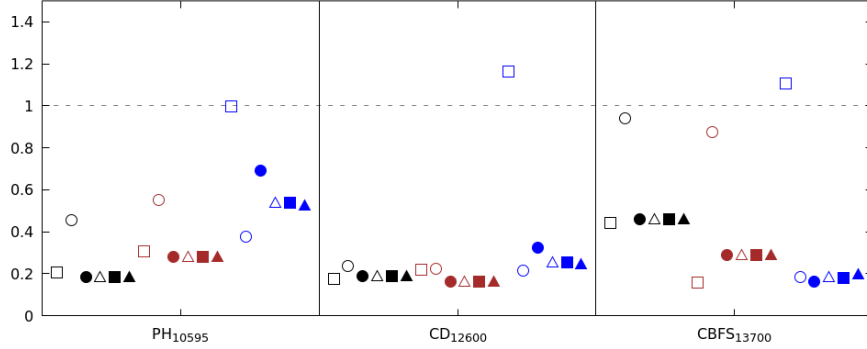


Figure 5: Cross-validation errors based on velocity profiles ( $\overline{u}_1$ ,  $\overline{u}_2$ ) for models trained on velocity and skin friction data. The errors are normalized with the mean-squared error of the baseline  $k-\omega$  SST model. Black : models trained on PH<sub>10595</sub>. Red : models trained on CD<sub>12600</sub>. Blue : models trained on CBFS<sub>13700</sub>.  $\square$  :  $\lambda = 10^{-2}$ .  $\circ$  :  $\lambda = 10^{-3}$ .  $\bullet$  :  $\lambda = 10^{-4}$ .  $\triangle$  :  $\lambda = 10^{-5}$ .  $\blacksquare$  :  $\lambda = 10^{-6}$ .  $\blacktriangle$  :  $\lambda = 10^{-7}$ .

The model with the lowest error averaged over the 3 test cases is the one learned on CD<sub>12600</sub> with  $\lambda = 10^{-2}$  and it is named  $M^{((U,Cf),CD,\lambda=10^{-2})}$  in the

following. Its mathematical expression involves 34 out of 36 candidate functions:

$$\begin{aligned}
b_{ij}^\Delta = & -(0.33155 + 1.4743I_1 + 1.1026I_2 + 0.84696I_1^2 + 0.79295I_1I_2 + 1.3092I_2^2)T_{ij}^{(1)} \\
& -(0.852670.33814I_1 + 1.4767I_2 + 1.3685I_1^2 + 1.516I_1I_2 + 0.15839I_2^2)T_{ij}^{(2)} \\
& -(0.82589 + 0.29539I_1 + 1.0474I_2 + 0.55784I_1^2 + 0.37194I_1I_2 + 0.3276I_2^2)T_{ij}^{(3)}
\end{aligned} \tag{23}$$

$$\begin{aligned}
b_{ij}^R = & -(0.23427 + 0.86596I_1 + 1.7198I_2 + 0.43626I_1^2 + 0.31858I_1I_2 + 1.1825I_2^2)T_{ij}^{(1)} \\
& -(0.69581I_1 + 0.81187I_2 + 1.43I_1^2 + 1.1061I_2^2)T_{ij}^{(2)} \\
& -(1.6195 + 0.52749I_1 + 0.2365I_2 + 0.32065I_1^2 + 1.1066I_1I_2 + 1.6107I_2^2)T_{ij}^{(3)}
\end{aligned} \tag{24}$$

We observe that the model is not very sparse even if a relatively high value of  $\lambda$  is used. This is likely an effect of the nonlinearity of the Navier–Stokes equations. Yet it generalizes well across the whole test set.

For both models we checked a posteriori that the realizability conditions are satisfied throughout the flow domain for all cases in the test and training sets, as we would have expected.

In the following, a detailed assessment of the two learned models against the high-fidelity data is carried out for a number of flow quantities, and the results are compared to those of the baseline LEVM model  $k\text{-}\omega$  SST. Additionally, we also report numerical results for the BSL-EARSM model of Menter et al. [23], as well as for a CFD-free SpaRTA model from [1], which is much more sparse:

$$b_{ij}^\Delta = 0 \tag{25}$$

$$b_{ij}^R = 0.39T_{ij}^{(1)} \tag{26}$$

and corresponds to a simple correction of the production terms in the  $k\text{-}\omega$  transport equations.

Finally, the learned models are applied to an unseen flow case not included in the training and testing datasets, namely the periodic hill flow at  $Re = 37000$ , and the results are compared to the reference data and to the models mentioned in the above.

## 5.2. Results for flow configurations in the training and test sets

The predictions of the discovered models  $M^{\tau,PH,\lambda=10^{-4}}$  and  $M^{((U,Cf),CD,\lambda=10^{-2})}$  for the 3 test cases are presented in figures 6, 7, 8 and 9 for the streamwise velocity  $\bar{u}_1$ , the turbulent kinetic energy  $k$ , the Reynolds shear stress  $\tau_{12}$  and the skin friction coefficient  $C_f$ , respectively. Their results are compared with those of the baseline  $k\text{-}\omega$  SST model, the CFD-free SpaRTA model, the BSL-EARSM model and the high-fidelity data. For a more quantitative evaluation we report in table 1 the mean squared errors on the longitudinal and wall-normal velocities, turbulent kinetic energy and Reynolds shear stress ( $\tau_{12}$ ) profiles, as well

as for the skin friction coefficient  $C_f$ , respectively. In all cases, the errors are normalized with the mean-squared error of the baseline  $k$ - $\omega$  SST model.

Table 1: Mean-squared errors of predicted velocity, turbulent kinetic energy and Reynolds shear-stress profiles and skin friction distribution with respect to high-fidelity data for various models. The errors are normalized by the mean-squared error of the baseline  $k$ - $\omega$  SST model.

Velocity ( $\bar{u}_1, \bar{u}_2$ )

	PH <sub>10595</sub>	CD <sub>12600</sub>	CBFS <sub>13700</sub>
$M(\tau, PH, \lambda=10^{-4})$	0.1847	0.1794	0.3589
$M((U, Cf), CD, \lambda=10^{-2})$	0.3079	0.2194	0.1595
CFD-free	0.2067	0.2067	0.1711
BSL-EARSM	0.3207	0.5999	0.7762

Turbulent kinetic energy  $k$

	PH <sub>10595</sub>	CD <sub>12600</sub>	CBFS <sub>13700</sub>
$M(\tau, PH, \lambda=10^{-4})$	0.8195	1.2187	1.5225
$M((U, Cf), CD, \lambda=10^{-2})$	0.7870	1.0556	1.1133
CFD-free	0.3478	0.7472	0.6135
BSL-EARSM	0.6881	0.9821	1.0065

Reynolds shear stress  $\tau_{12}$

	PH <sub>10595</sub>	CD <sub>12600</sub>	CBFS <sub>13700</sub>
$M(\tau, PH, \lambda=10^{-4})$	0.5014	0.9573	0.9913
$M((U, Cf), CD, \lambda=10^{-2})$	0.5736	0.9418	0.7717
CFD-free	0.5535	0.9394	0.7162
BSL-EARSM	1.2229	0.9524	0.8061

Skin friction coefficient  $C_f$

	PH <sub>10595</sub>	CD <sub>12600</sub>	CBFS <sub>13700</sub>
$M(\tau, PH, \lambda=10^{-4})$	2.0941	0.5415	1.2924
$M((U, Cf), CD, \lambda=10^{-2})$	1.4927	0.5883	0.3490
CFD-free	2.05082	0.5958	0.3125
BSL-EARSM	2.5022	0.6383	0.2203

Both discovered models drastically improve of velocity with respect to the  $k$ - $\omega$ -SST and the BSL-EARSM models, particularly within the separated regions (see figure 6). Furthermore, their accuracy is similar to the CFD-free SpARTA. The model learned using high fidelity velocity profiles and skin friction training data provide a lower average error (over the three test cases) for the velocity profiles prediction than the model learned using high fidelity Reynolds stress profiles as training data.

The discovered models improve the prediction of  $k$  profiles over the LEVM for the case PH<sub>10595</sub>. Inspection of figure 7 and table 1 shows that model  $M(\tau, PH, \lambda=10^{-4})$  provides a higher error for  $k$  for cases CD<sub>12600</sub> and CBFS<sub>13700</sub>,

while model  $M^{((U,Cf),CD,\lambda=10^{-2})}$  has sensibly the same accuracy than the  $k-\omega$ -SST model for  $CD_{12600}$  and a slightly higher error for  $CBFS_{13700}$ . The accuracy of both discovered models is however comparable with the BSL-EARSM model for this quantity of interest. Remarkably, the model trained against velocity profiles and skin friction provides better predictions of  $k$  than the model using Reynolds stress data. The CFD-free model, which uses high-fidelity data for  $k$  in the training prediction of the production correction  $R$  improves the results for the three test cases.

Model  $M^{((U,Cf),CD,\lambda=10^{-2})}$  improves the prediction of  $\tau_{12}$  (see figure 8) for the three test cases and outperforms  $M^{(\tau,PH,\lambda=10^{-4})}$  also for this quantity of interest. The accuracy of the discovered models is comparable to the accuracy of the CFD-free model for the prediction of  $\tau_{12}$ , while the BSL-EARSM model deteriorates the prediction of  $\tau_{12}$  for  $PH_{10595}$ , only slightly improves the results for  $CD_{12600}$  and is more accurate than the LEVM only for case  $CBFS_{13700}$ .

The skin friction means square errors of all models are higher than the  $k-\omega$ -SST for case  $PH_{10595}$ , the best results being once again achieved with  $M^{((U,Cf),CD,\lambda=10^{-2})}$ . This is due to the very high skin friction peak obtained on the windward side of the hill for all models. Nevertheless all EARSM models drastically improve the prediction of the reattachment point location as shown in table 2. Additionally, all models improve the prediction of the skin friction for  $CD_{12600}$  on average, although none of them captures the small recirculation bubble predicted by the DNS accurately. Model  $M^{((U,Cf),CD,\lambda=10^{-2})}$  also improves the prediction of the skin friction distribution and provides sensibly the same accuracy than the CFD-free and the BSL-EARSM model for  $CBFS_{13700}$ , while  $M^{(\tau,PH,\lambda=10^{-4})}$  performs worst than the  $k-\omega$ -SST model. Again, this is balanced by the drastically improved predictions of the separation and reattachment locations. This results shows the sensitivity of the CFD-driven method with respect to the training data. Indeed,  $M^{((U,Cf),CD,\lambda=10^{-2})}$  outperforms  $M^{(\tau,PH,\lambda=10^{-4})}$  for all quantities of interest.

In summary, all data-driven models are overall more accurate than the baseline LEVM and the BSL-EARSM for cases in the training and test sets. The CFD-free model is somewhat more accurate than the CFD-driven ones. This model uses however much more data for training, including full turbulent kinetic energy and velocity fields used to determine the  $R$  corrective term. To better discriminate among the learned models, in the next Section we evaluate their extrapolation performance to a flow configuration outside the training and test sets.

Table 2: Predicted separation and reattachment points ( $x/h$ ) for various models.

Separation points		
	PH <sub>10595</sub>	CBFS <sub>13700</sub>
LES	0.2154	0.9429
k- $\omega$ SST	0.2696	0.7655
$M^{(\tau,PH,\lambda=10^{-4})}$	0.2793	1.1510
$M^{((U,Cf),CD,\lambda=10^{-2})}$	0.2750	0.9819
CFD-free	0.2845	1.0503
BSL-EARSM	0.2817	0.8181

Reattachment points		
	PH <sub>10595</sub>	CBFS <sub>13700</sub>
LES	4.7595	4.2409
k- $\omega$ SST	7.6418	6.0296
$M^{(\tau,PH,\lambda=10^{-4})}$	4.5664	3.9726
$M^{((U,Cf),CD,\lambda=10^{-2})}$	5.4135	4.5224
CFD-free	5.0115	4.4754
BSL-EARSM	4.5613	5.1107

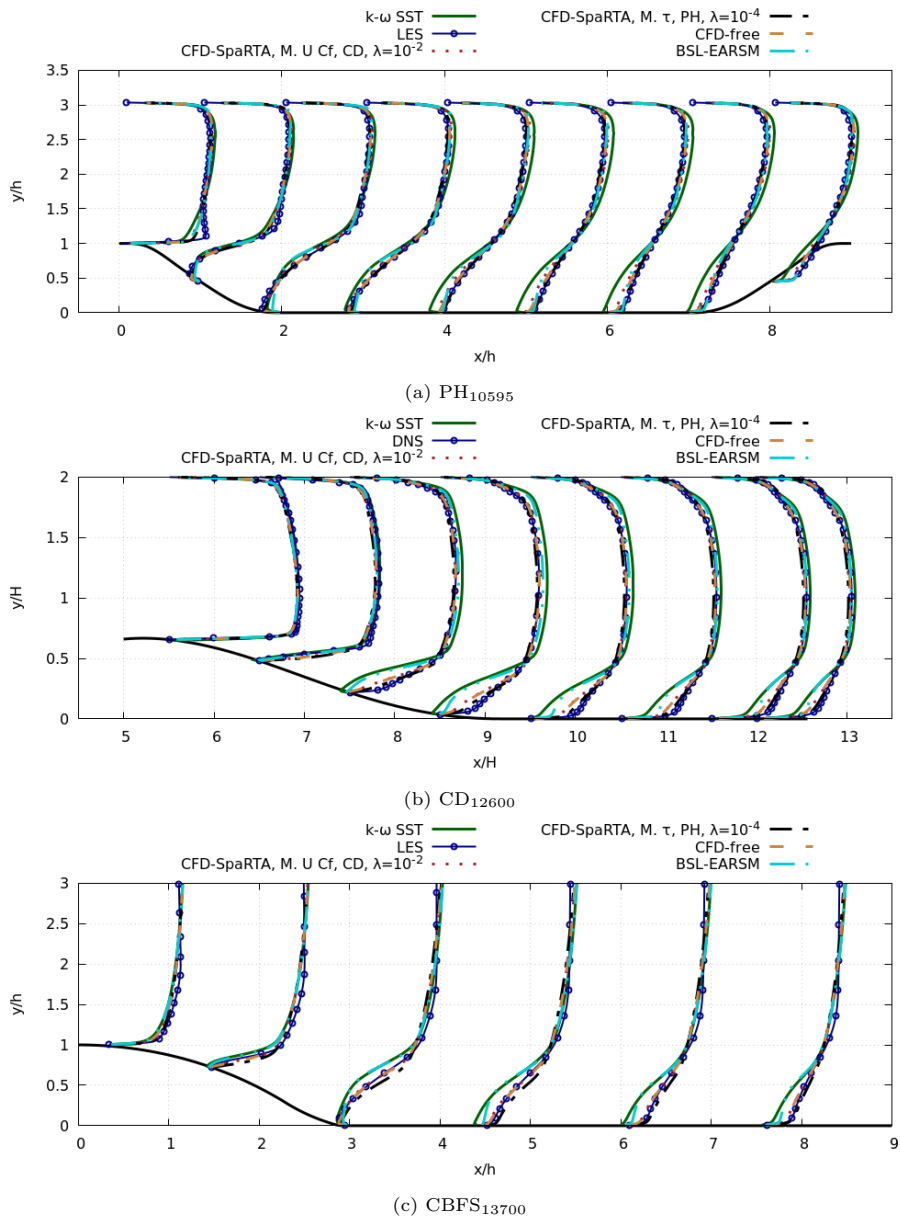


Figure 6: Assessment of various CFD-driven, CFD-free and standard turbulence models for flows in the training and test set: streamwise velocity profiles ( $\overline{u_1}/U_b + x/h$ ).

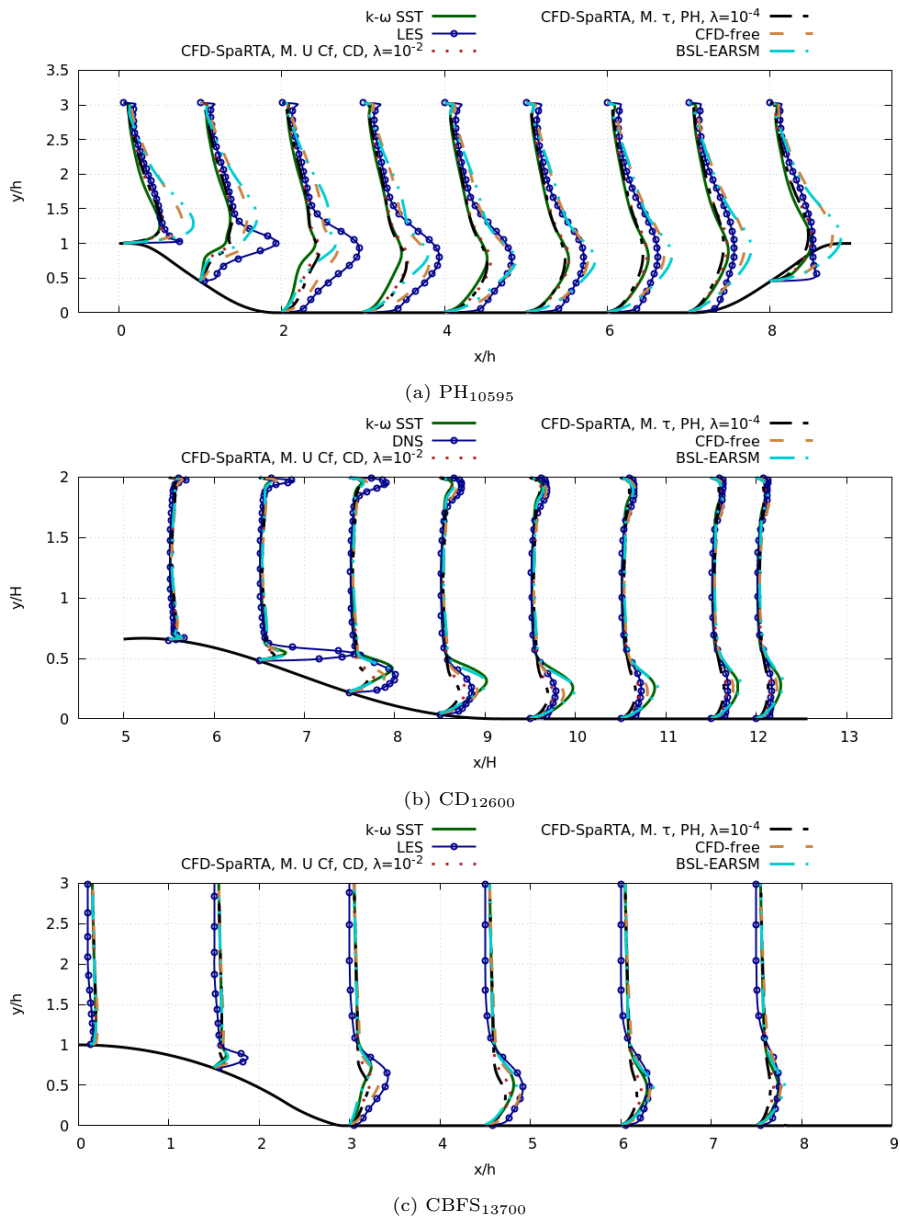


Figure 7: Assessment of various CFD-driven, CFD-free and standard turbulence models for flows in the training and test set: turbulent kinetic energy profiles ( $12k/U_b^2 + x/h$ ).

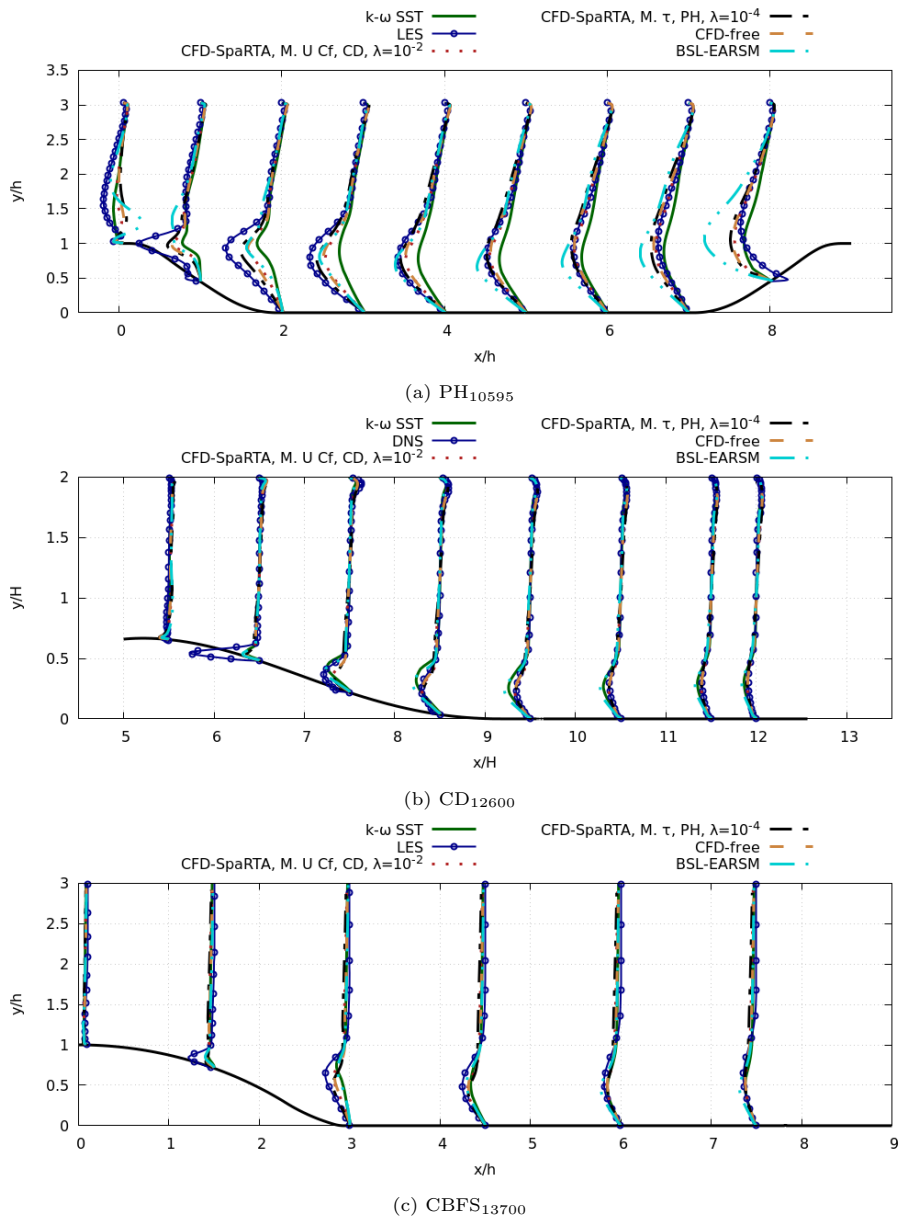
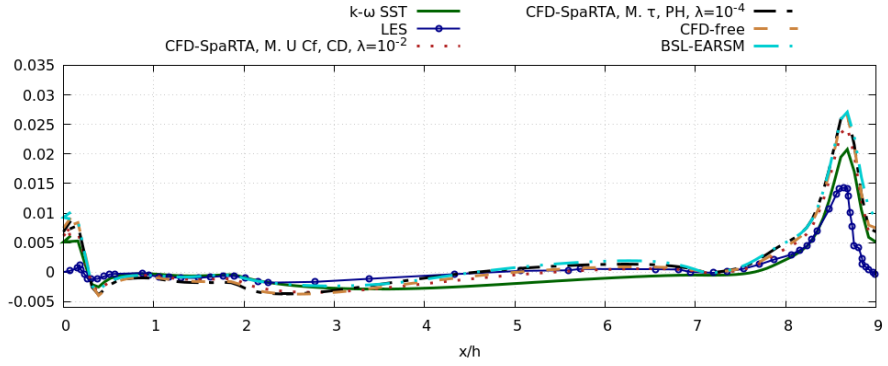
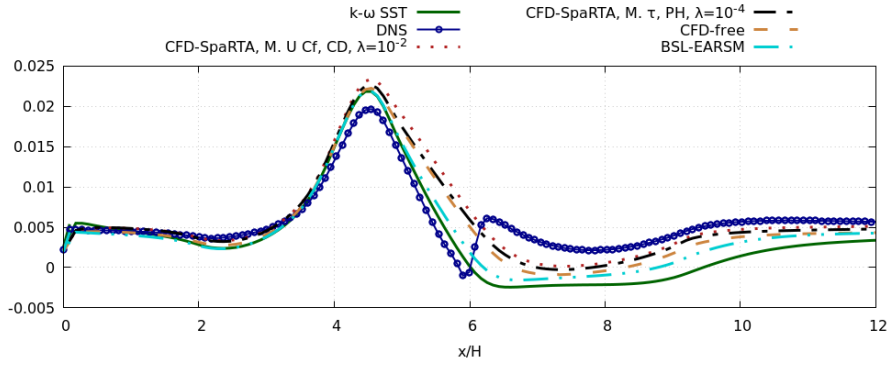


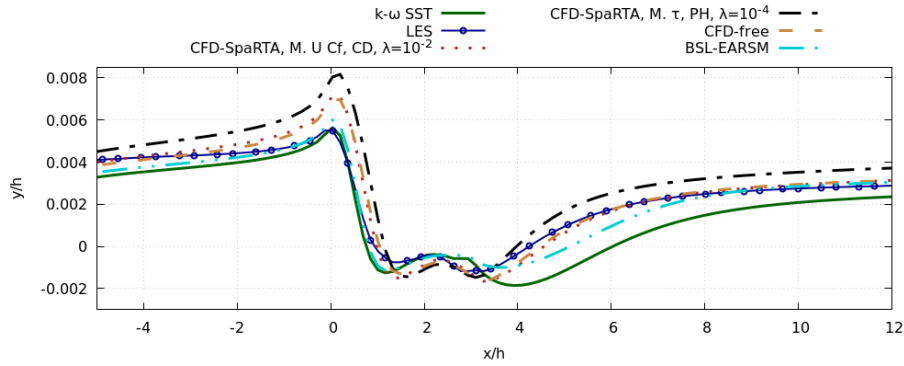
Figure 8: Assessment of various CFD-driven, CFD-free and standard turbulence models for flows in the training and test set: Reynolds shear stress profiles ( $20\tau_{12}/U_b^2 + x/h$ ).



(a) PH<sub>10595</sub>



(b) CD<sub>12600</sub>



(c) CBFS<sub>13700</sub>

Figure 9: Assessment of various CFD-driven, CFD-free and standard turbulence models for flows in the training and test set: skin friction distributions along the bottom wall.

### 5.3. Extrapolation to an unseen flow

To test the ability of the CFD-driven SpaRTA to serve as a predictive model for 2D turbulent flow with separations, the two CFD-driven models learned for cases PH<sub>10595</sub>, CD<sub>12600</sub> and CBFS<sub>13700</sub> are applied to the 2D periodic hill flow

case at  $\text{Re}=37000$  (noted  $\text{PH}_{37000}$ ). For model  $M^{(\tau,PH,\lambda=10^{-4})}$ , the simulation of  $\text{PH}_{37000}$  represents an extrapolation to a higher Reynolds number, while for  $M^{((U,Cf),CD,\lambda=10^{-2})}$ , both the Reynolds number and the geometry are different, even if the flow still belongs to the class of 2D incompressible separated flow in a variable section channel. The results for the streamwise velocity  $\bar{u}_1$ , the turbulent kinetic energy  $k$ , the Reynolds shear stress  $\tau_{12}$  and the skin friction coefficient  $C_f$  are compared to LES data from [38] in figures 10, 11, 12 and 13, respectively. The results of the baseline LEVM, of the BSL-EARSM and of the CFD-free SpaRTA model are also reported for comparison.

Table 3: Mean-squared errors of predicted velocity, turbulent kinetic energy and Reynolds shear-stress profiles and skin friction distribution with respect to high-fidelity data for various models applied to the PH case at  $\text{Re}=37000$ . The errors are normalized by the mean-squared error of the baseline  $k-\omega$  SST model.

	$\bar{u}_1, \bar{u}_2$	$k$	$\tau_{12}$	$C_f$
$M^{(\tau,PH,\lambda=10^{-4})}$	0.2130	0.6422	0.6594	0.8704
$M^{((U,Cf),CD,\lambda=10^{-2})}$	0.4580	0.8041	0.7168	0.8133
CFD-free	0.3280	2.5153	0.6841	0.9292
BSL-EARSM	0.4380	3.7959	1.4510	0.9912

The normalized mean squared errors with respect to the high-fidelity data from [38] are reported in table 3 and the predicted separation and reattachment points are given in table 4.

Model  $M^{(\tau,PH,\lambda=10^{-4})}$  significantly improves of the predictions of all quantities of interest, including  $k$ , showing his ability to improve the accuracy of the baseline  $k-\omega$  SST even at a higher Reynolds number. Model  $M^{(\tau,CD,\lambda=10^{-2})}$ , learned on  $\text{CD}_{12600}$ , which is doubly extrapolated in both Reynolds and geometry, is slightly less accurate than  $M^{(\tau,PH,\lambda=10^{-4})}$  but still performs better than the LEVM. For the present extrapolation case, the CFD-free SpaRTA provides slightly less accurate but yet comparable prediction than the CFD-driven models, but it does not extrapolate well for  $k$ , for which the error is more than twice larger than the baseline LEVM. BSL-EARSM provides a poor prediction of  $k$  for all cases.

These results show that the CFD-driven models robustly improve predictive accuracy of the  $k-\omega$  SST model also for a 2D separated flow outside the training set and exhibit a better extrapolation performance than the CFD-free SpaRTA.

Table 4: Predicted separation and reattachment points ( $x/h$ ) for various models.

	separation	reattachment
LES	0.2552	4.0170
k- $\omega$ SST	0.2679	7.5479
$M(\tau, PH, \lambda=10^{-4})$	0.2941	4.0851
$M((U, Cf), CD, \lambda=10^{-2})$	0.2816	4.9646
CFD-free	0.2951	4.6303
BSL-EARSM	0.2898	4.2333

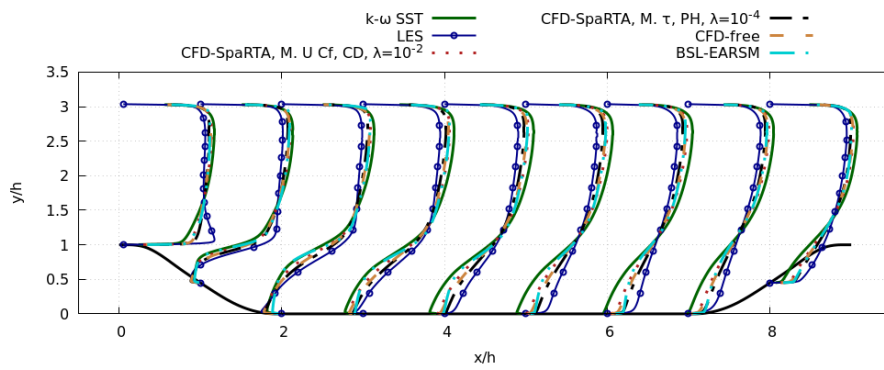


Figure 10: Longitudinal velocity profiles normalized with bulk velocity :  $\overline{u}_1/U_b + x$  for  $PH_{37000}$ .

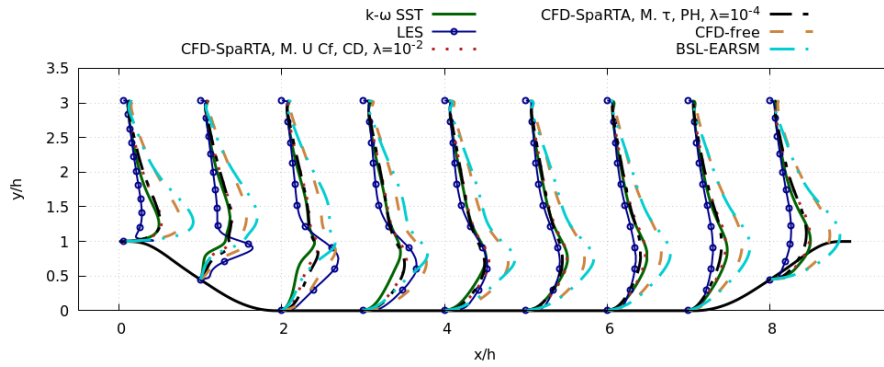


Figure 11: Turbulent kinetic energy profiles normalized with bulk velocity :  $12k/U_b^2 + x$  for  $PH_{37000}$ .

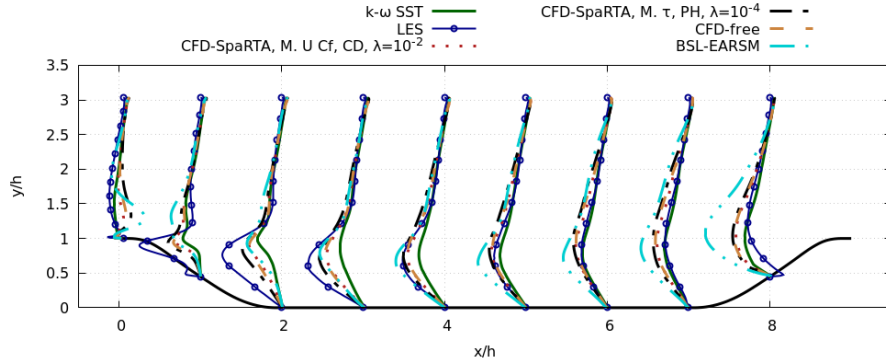


Figure 12: Reynolds shear stress profiles normalized with bulk velocity :  $20\tau_{12}/U_b^2 + x$  for PH<sub>37000</sub>.

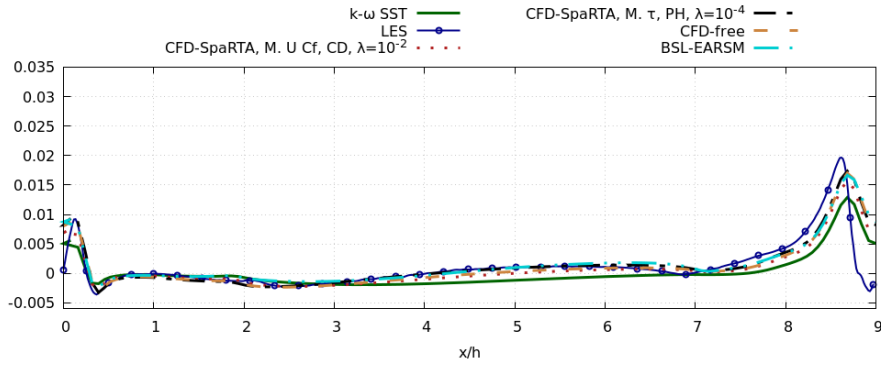


Figure 13: Skin friction distribution  $C_f$  for PH<sub>37000</sub>.

## 6. Conclusions

A CFD-driven counterpart of the SpaRTA method initially proposed in [1] has been presented. The new method aims at discovering data-augmented EARSMS with improved performance for a given class of flows with respect to a baseline LEVM through deterministic symbolic identification of terms from a predefined library of candidate functions. As in SpaRTA, the discovered models use a generalized eddy viscosity formulation in conjunction with corrective terms for the production of the transported turbulent variables. The CFD-driven approach is intended to overcome limitations of the CFD-free model discovery in terms of numerical robustness of the learned models and to enable flexible use of any kind of data for model training. Importantly, the CFD-driven approach does not necessarily require data for second-order turbulence statistics, namely, the Reynolds stresses, which are not always easily available, e.g., in experimental data sets.

In the present work we focused on correcting the  $k-\omega$  SST model for a class of 2D turbulent flows with separations caused by an enlargement of the channel section. The methodology may however be adapted to other eddy viscosity models and different flow configurations. The present test cases include the well-known periodic hill flow, a converging-diverging channel and the flow behind a curved backward facing step, for which high-fidelity DNS or LES data are available in the literature. To show the ability of the CFD-driven method to train models with any kind of data, two sets of high-fidelity data have been considered. First, models are discovered using data for Reynolds stress profiles at a few streamwise locations. Second, we prove the flexibility of the proposed approach by training models against selected velocity profiles and skin friction data.

The computational cost of CFD-driven model identification is obviously much higher than CFD-free training. To speed up the learning process, we use a surrogate model for solving the optimization problem. In this way, a complete model identification run, including model training and selection via cross-validation, requires  $O(1000)$  CFD solves, which remains affordable even on a standard workstation. For more complex 3D cases, a parallelization of the CFD solves can be implemented in a straightforward manner.

The CFD-driven discovered models are numerically robust, thanks to the CFD-driven training and regularization constraints on model parameters. They are shown to satisfy realizability conditions throughout the computational domain. For flow configurations in the training and test sets, they exhibit improved accuracy not only over the baseline LEVM, but also over a general purpose EARSIM model [23] and they have an accuracy comparable to a data-driven model generated with the CFD-free SpARTA algorithm, which employs full-field velocity and Reynolds stress data. The model learned from velocity and skin friction data is slightly more accurate than the one trained on Reynolds stress data for most quantities of interest. The CFD-driven models have then been applied to a separated flow outside the training and test sets, characterized by a higher Reynolds number and a different geometry. For this configuration, the learned models provide significantly improved results for most flow quantities of interest, not only over the baseline  $k-\omega$  model but also over the general purpose BLS-EARSIM model. For the extrapolation case, the CFD-free SpARTA model is found to be less accurate than the CFD-driven ones, although it still performs better than the baseline LEVM.

In conclusion, the CFD-driven SpARTA represent a promising method to generate data-driven EARSIMs. The computational overcost of the training algorithm is justified by the possibility of using any kind of available data, including incomplete data sets, as those potentially obtained from experiments. Furthermore, such models are by construction numerically robust. Finally, they are found to extrapolate better than CFD-free models to flow configurations outside the training set.

## 7. Acknowledgements

The present work was carried out in the frame of project PERTINENT (high-fidelity exPERimental and numERical study for daTa-drIven modeliNg of rEalistic turbuleNt separaTed flows), funded by Institut Carnot ARTS, France.

## References

- [1] M. Schmelzer, R. P. Dwight, P. Cinnella, Discovery of algebraic reynolds-stress models using sparse symbolic regression, *Flow, Turbulence and Combustion* 104 (2) (2020) 579–603.
- [2] D. C. Wilcox, et al., *Turbulence modeling for CFD*, Vol. 3rd Edition, DCW industries La Canada, CA, 2006.
- [3] A. Hellsten, S. Wallin, Explicit algebraic reynolds stress and non-linear eddy-viscosity models, *International Journal of Computational Fluid Dynamics* 23 (4) (2009) 349–361.
- [4] B. E. Launder, G. J. Reece, W. Rodi, Progress in the development of a reynolds-stress turbulence closure, *Journal of fluid mechanics* 68 (3) (1975) 537–566.
- [5] S. B. Pope, *Turbulent flows* (2001).
- [6] H. K. Versteeg, W. Malalasekera, *An introduction to computational fluid dynamics: the finite volume method*, Pearson education, 2007.
- [7] S. Pope, A more general effective-viscosity hypothesis, *Journal of Fluid Mechanics* 72 (2) (1975) 331–340.
- [8] T. B. Gatski, C. G. Speziale, On explicit algebraic stress models for complex turbulent flows, *Journal of Fluid Mechanics* 254 (1993) 59–78. doi:10.1017/S0022112093002034.
- [9] X. Heng, P. Cinnella, Quantification of model uncertainty in rans simulations: A review, *Progress in Aerospace Sciences* 108 (2019) 1–31.
- [10] K. Duraisamy, G. Iaccarino, H. Xiao, Turbulence modeling in the age of data, *Annual Review of Fluid Mechanics* 51, doi: 10.1146/annurev-fluid-010518-040547 (2019).
- [11] J. Weatheritt, R. Sandberg, A novel evolutionary algorithm applied to algebraic modifications of the rans stress-strain relationship, *Journal of Computational Physics* 325 (2016) 22–37.
- [12] J. Weatheritt, R. Sandberg, The development of algebraic stress models using a novel evolutionary algorithm, *International Journal of Heat and Fluid Flow* 68 (2017) 298–318.

- [13] H. D. Akolekar, J. Weatheritt, N. Hutchins, R. D. Sandberg, G. Laskowski, V. Michelassi, Development and use of machine-learnt algebraic reynolds stress models for enhanced prediction of wake mixing in low-pressure turbines, *Journal of Turbomachinery* 141 (4) (2019).
- [14] S. L. Brunton, J. L. Proctor, J. N. Kutz, Discovering governing equations from data by sparse identification of nonlinear dynamical systems, *Proceedings of the national academy of sciences* 113 (15) (2016) 3932–3937.
- [15] S. H. Rudy, S. L. Brunton, J. L. Proctor, J. N. Kutz, Data-driven discovery of partial differential equations, *Science Advances* 3 (4) (2017) e1602614.
- [16] Y. Zhang, R. Dwight, M. Schmelzer, J. Gómez, Z.-H. Han, S. Hickel, Customized data-driven rans closures for bi-fidelity les-rans optimization, *Journal of Computational Physics* 432 (2021) 110153. doi:10.1016/j.jcp.2021.110153.
- [17] S. Beetham, J. Capecelatro, Formulating turbulence closures using sparse regression with embedded form invariance, *Physical Review Fluids* 5 (08 2020). doi:10.1103/PhysRevFluids.5.084611.
- [18] J. Ling, A. Kurzawski, J. Templeton, Reynolds averaged turbulence modelling using deep neural networks with embedded invariance, *Journal of Fluid Mechanics* 807 (2016) 155–166. doi:10.1017/jfm.2016.615.
- [19] Y. Zhao, H. D. Akolekar, J. Weatheritt, V. Michelassi, R. D. Sandberg, Rans turbulence model development using cfd-driven machine learning, *Journal of Computational Physics* 411 (2020) 109413.
- [20] S. Banerjee, R. Krahl, F. Durst, C. Zenger, Presentation of anisotropy properties of turbulence, invariants versus eigenvalue approaches, *Journal of Turbulence* (8) (2007) N32.
- [21] R. G. Regis, C. A. Shoemaker, Constrained global optimization of expensive black box functions using radial basis functions, *Journal of Global optimization* 31 (1) (2005) 153–171.
- [22] M. F.R., Two-equation eddy-viscosity turbulence model for engineering applications, *AIAA Journal* 32 (1994) 1598–1605.
- [23] F. Menter, A. Garbaruk, Y. Egorov, Explicit algebraic reynolds stress models for anisotropic wall-bounded flows, *Progress in Flight Physics* 3 (2012) 89–104.
- [24] H. G. Weller, G. Tabor, H. Jasak, C. Fureby, A tensorial approach to computational continuum mechanics using object-oriented techniques, *Computers in physics* 12 (6) (1998) 620–631.

- [25] L. Caretto, A. Gosman, S. Patankar, D. Spalding, Two calculation procedures for steady, three-dimensional flows with recirculation, in: Proceedings of the third international conference on numerical methods in fluid mechanics, Springer, 1973, pp. 60–68.
- [26] M. Breuer, N. Peller, C. Rapp, M. Manhart, Flow over periodic hills—numerical and experimental study in a wide range of reynolds numbers, *Computers & Fluids* 38 (2) (2009) 433–457.
- [27] M. Marquillie, U. Ehrenstein, J.-P. Laval, et al., Instability of streaks in wall turbulence with adverse pressure gradient, *Journal of Fluid Mechanics* 681 (205-240) (2011) 30.
- [28] Y. Bentaleb, S. Lardeau, M. A. Leschziner, Large-eddy simulation of turbulent boundary layer separation from a rounded step, *Journal of Turbulence* (13) (2012) N4.
- [29] S. L. Brunton, J. N. Kutz, *Data-driven science and engineering: Machine learning, dynamical systems, and control*, Cambridge University Press, 2019.
- [30] T. McConaghy, Ffx: Fast, scalable, deterministic symbolic regression technology, in: *Genetic Programming Theory and Practice IX*, Springer, 2011, pp. 235–260.
- [31] C. M. Bishop, *Pattern recognition and machine learning*, springer, 2006.
- [32] P. Knysh, Y. Korkolis, Blackbox: A procedure for parallel optimization of expensive black-box functions, *arXiv preprint arXiv:1605.00998* (2016).
- [33] C. G. Speziale, R. Abid, P. A. Durbin, On the realizability of reynolds stress turbulence closures, *Journal of Scientific Computing* 9 (4) (1994) 369–403.
- [34] M. Emory, G. Iaccarino, Visualizing turbulence anisotropy in the spatial domain with componentality contours, *Center for Turbulence Research Annual Research Briefs* (2014) 123–138.
- [35] W. N. Edeling, G. Iaccarino, P. Cinnella, Data-free and data-driven rans predictions with quantified uncertainty, *Flow, Turbulence and Combustion* 100 (3) (2018) 593–616.
- [36] M. Kommenda, B. Burlacu, G. Kronberger, M. Affenzeller, Parameter identification for symbolic regression using nonlinear least squares, *Genetic Programming and Evolvable Machines* 21 (2020) 471–501. doi:<https://doi.org/10.1007/s10710-019-09371-3>.
- [37] Z. Yang, Z. Wang, H. Liu, Y. Eldar, T. Zhang, Sparse nonlinear regression: Parameter estimation under nonconvexity, in: M. F. Balcan, K. Q. Weinberger (Eds.), *Proceedings of The 33rd International Conference on Machine Learning*, Vol. 48 of *Proceedings of Machine Learning Research*,

PMLR, New York, New York, USA, 2016, pp. 2472–2481.  
URL <http://proceedings.mlr.press/v48/yangc16.html>

- [38] X. Gloerfelt, P. Cinnella, Large eddy simulation requirements for the flow over periodic hills, *Flow, Turbulence and Combustion* 103 (1) (2019) 55–91.
- [39] S. Wallin, A. V. Johansson, An explicit algebraic reynolds stress model for incompressible and compressible turbulent flows, *Journal of Fluid Mechanics* 403 (2000) 89–132.
- [40] P. A. Durbin, Near-wall turbulence closure modeling without “damping functions”, *Theoretical and computational fluid dynamics* 3 (1) (1991) 1–13.

### Appendix A. The $k$ - $\omega$ SST model

Transport equations of  $k$  and  $\omega$  write :

$$\frac{\partial k}{\partial t} + U_j \frac{\partial k}{\partial x_j} = P_k - \beta^* k \omega + \frac{\partial}{\partial x_j} [(\nu + \sigma_k \nu_t) \frac{\partial k}{\partial x_j}] \quad (\text{A.1})$$

$$\frac{\partial \omega}{\partial t} + U_j \frac{\partial \omega}{\partial x_j} = \frac{\gamma}{\nu_t} P_k - \beta \omega^2 + \frac{\partial}{\partial x_j} [(\nu + \sigma_\omega \nu_t) \frac{\partial \omega}{\partial x_j}] + CD_{k\omega}, \quad (\text{A.2})$$

with  $P_k = -2\nu_t S_{ij} \partial_j U_i$ . The corresponding eddy viscosity writes

$$\nu_t = \frac{a_1 k}{\max(a_1 \omega, SF_2)}. \quad (\text{A.3})$$

The other standard terms read

$$\begin{aligned} CD_{k\omega} &= \max(2\sigma_\omega^2 \frac{1}{\omega} (\partial_i k) (\partial_i \omega), 10^{-10}), \\ F_1 &= \tanh[(\min[\max(\frac{\sqrt{k}}{\beta^* \omega y}, \frac{500\nu}{y^2 \omega}), \frac{4\sigma_\omega^2 k}{CD_{k\omega} y^2}])]^4, \\ F_2 &= \tanh[(\max(\frac{2\sqrt{k}}{\beta^* \omega y}, \frac{500\nu}{y^2 \omega}))^2], \\ \Phi &= F_1 \Phi_1 + (1 - F_1) \Phi_2, \end{aligned} \quad (\text{A.4})$$

in which the latter blends the coefficients  $\Phi \rightarrow (\Phi_1, \Phi_2)$

$$\alpha = (5/9, 0.44), \quad \beta = (3/40, 0.0828), \quad \sigma_k = (0.85, 1.0), \quad \sigma_\omega = (0.5, 0.856). \quad (\text{A.5})$$

The remaining terms are  $\beta^* = 0.09$ ,  $a_1 = 0.31$ .

## Appendix B. The BSL-EARSMmodel

We here recall the formulation of the BSL-EARSM of Menter et al. [23]. This model is based on the EARSM formulation of Wallin and Johansson [39] (WJ model) for the stress-strain relationship. In the WJ model, the stress-strain relationship is combined with the  $k$ - $\omega$  transport equations of Wilcox [2]. In the BSL-EARSM, in order to avoid the freestream sensitivity of the Wilcox model, the WJ stress-strain relationship is combined with the BSL  $k$ - $\omega$  model of Menter [22].

Following [7], the Reynolds stress anisotropy tensor  $a_{ij}$  is projected onto a tensor basis :

$$a_{ij} = \beta_1 T_{1,ij} + \beta_2 T_{2,ij} + \beta_3 T_{3,ij} + \beta_4 T_{4,ij} + \beta_6 T_{6,ij} + \beta_9 T_{9,ij}, \quad (\text{B.1})$$

where

$$\begin{aligned} T_{1,ij} &= S_{ij}^*; & T_{2,ij} &= S_{ik}^* S_{kj}^* - \frac{1}{3} I_1 \delta_{ij}; & T_{3,ij} &= \Omega_{ik}^* \Omega_{kj}^* - \frac{1}{3} I_2 \delta_{ij}; \\ T_{4,ij} &= S_{ik}^* \Omega_{kj}^* - \Omega_{ik}^* S_{kj}^*; & T_{6,ij} &= S_{ik}^* \Omega_{kl}^* \Omega_{lj}^* + \Omega_{ik}^* \Omega_{kl}^* S_{lj}^* - \frac{2}{3} I_4 \delta_{ij} - I_2 S_{ij}^*; \\ T_{9,ij} &= \Omega_{ik}^* S_{kl}^* \Omega_{lm}^* \Omega_{mj}^* - \Omega_{ik}^* \Omega_{kl}^* S_{lm}^* \Omega_{mj}^* + \frac{1}{2} I_2 (S_{ik}^* \Omega_{kj}^* - \Omega_{ik}^* S_{kj}^*), \end{aligned} \quad (\text{B.2})$$

with  $S_{ij}^*$  and  $\Omega_{ij}^*$ , the non-dimensional mean strain rate and rotation rate defined as follows :

$$S_{ij}^* = \frac{\tau}{2} \left( \frac{\partial U_i}{\partial x_j} + \frac{\partial U_j}{\partial x_i} \right), \quad \Omega_{ij}^* = \frac{\tau}{2} \left( \frac{\partial U_i}{\partial x_j} - \frac{\partial U_j}{\partial x_i} \right) \quad (\text{B.3})$$

where  $\tau$  is a turbulent time scale with a Kolmogorov limiter [40]:

$$\tau = \max\left(\frac{1}{C_\mu \omega}, 6 \sqrt{\frac{\nu}{C_\mu k \omega}}\right). \quad (\text{B.4})$$

The tensor invariants  $I_1$ ,  $I_2$  and  $I_4$  read:

$$I_1 = S_{ij}^* S_{ji}^*, \quad I_2 = \Omega_{ij}^* \Omega_{ji}^*, \quad I_4 = S_{ik}^* \Omega_{kj}^* \Omega_{ji}^*. \quad (\text{B.5})$$

The coefficients of the tensor basis  $\beta_i$  in B.1 are defined as :

$$\beta_1 = -\frac{N}{Q}, \quad \beta_2 = 0, \quad \beta_3 = -\frac{2I_4}{NQ_1}, \quad \beta_4 = -\frac{1}{Q}, \quad \beta_6 = -\frac{N}{Q_1}, \quad \beta_9 = \frac{1}{Q_1}, \quad (\text{B.6})$$

with

$$Q = \frac{(N^2 - 2I_2)}{A_1}, \quad Q_1 = \frac{Q}{6} (2N^2 - I_2) \quad (\text{B.7})$$

where

$$N = C'_1 + \frac{9 \tilde{P}_k}{4 \epsilon} \quad (\text{B.8})$$

and

$$A_1 = 1.2, \quad C'_1 = \frac{9}{4}(C_1 - 1) \quad \text{and} \quad C_1 = 1.8. \quad (\text{B.9})$$

$N$  is a solution of the cubic equation :

$$N^3 - C'_1 N^2 - (2.7I_1 + 2I_2)N + 2C'_1 I_2 = 0 \quad (\text{B.10})$$

which is given by :

$$\begin{cases} N = \frac{C'_1}{3} + (P_1 + \sqrt{P_2})^{1/3} + \text{sign}(P_1 - \sqrt{P_2}) |P_1 - \sqrt{P_2}|^{1/3} & \text{at } P_2 \geq 0 \\ N = \frac{C'_1}{3} + 2(P_1^2 - P_2)^{1/6} \cos(\frac{1}{3} \arccos(\frac{P_1}{\sqrt{P_1^2 - P_2}})) & \text{at } P_2 < 0 \end{cases} \quad (\text{B.11})$$

with

$$P_1 = C'_1 \left( \frac{C_1'^2}{27} + \frac{9}{20} I_1 - \frac{2}{3} I_2 \right), \quad P_2 = P_1^2 - \left( \frac{C_1'^2}{9} + \frac{9}{10} I_1 + \frac{2}{3} I_2 \right)^3. \quad (\text{B.12})$$

The BSL-EARSM constitutive equation is then supplemented by transport equations for  $k$  and  $\omega$ . These are the same as in Appendix A, where a modified production term is used:

$$\tilde{P}_k = \min(-\tau_{ij} \frac{\partial U_i}{\partial x_j}, 10. \rho \beta^* k \omega). \quad (\text{B.13})$$

The reader is referred to [23] for further details.

### Appendix C. CORS algorithm

The main steps of the algorithm proceed as follows:

- The total number of function evaluations, noted  $N$ , is set from the beginning. It must satisfy the condition  $N > 2D$ , where  $D$  is the dimensionality of the search space.

- Initial step :

- An initial sampling of size  $N/2$  of the parameter space  $S_1 = \{\hat{\Theta}_i | i = 1, 2, \dots, N/2\}$  is performed using the Latin Hypercube sampling method.
- An initial response surface  $\hat{f}_1$  is constructed using cubic radial basis functions (RBF) and the initial sampling  $S_1$ . The functions are of the form:

$$\hat{f}_1(\hat{\Theta}) = \sum_{i=1}^{N/2} \lambda_i \phi(\|\hat{\Theta} - \hat{\Theta}_i\|) + b^T \hat{\Theta} + a, \quad (\text{C.1})$$

where  $\phi$  is a cubic function ( $\phi(r) = r^3$ ) and  $\lambda_i$ ,  $b$  and  $a$  are coefficients determined by interpolating the available samples.

- Steps 1 to  $N/2$ :
  - The candidate sample  $\hat{\Theta}_i$  minimizing the surface response  $\hat{f}_{i-1}$  is selected. In order to prevent the algorithm from being trapped in a local minimum, a ball of radius  $r$  is placed around each of previously sampled points and the candidate sample minimizing the surface response is required to be outside of any ball.
  - The cost function is evaluated for  $\hat{\Theta}_i$ .
  - A new response surface  $\hat{f}_i$  is constructed using the sampling  $S_{i-1} \cup \hat{\Theta}_i$ .

The last candidate sample  $\hat{\Theta}_N$  is the solution of the problem proposed by the algorithm.